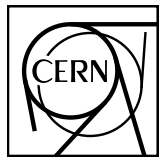


EUROPEAN ORGANIZATION FOR NUCLEAR RESEARCH

1



ALICE-ANA-XXXX
Tuesday 21st May, 2019

2

3

Constraining anti-deuteron inelastic interaction cross-section via \bar{d}/d ratio in p–Pb collisions at $\sqrt{s_{NN}} = 5.02 \text{ TeV}$

4

5

I. Vorobyev¹, L. Cordova Nyffenegger¹, A. Dashi¹, L. Fabbietti¹

6

1. Technische Universität München, Physik Department

7

Email: ivan.vorobyev@cern.ch, lucas.cordova.nyffenegger@cern.ch,
anisa.dashi@cern.ch, laura.fabbietti@ph.tum.de

8

Abstract

9

Low-energy anti-deuterons could be a unique probe for indirect search of Dark Matter annihilation performed currently by several experiments placed on satellites or balloons. The interaction cross-sections of (anti-)deuterons with matter, however, are known very poorly by today, with only a few experimental data points for scattering on some materials available in the momentum region below $p \sim 20 \text{ GeV}/c$. At the same time, matter and anti-matter are produced at the LHC collision energies in almost equal amounts, allowing us to study the production cross-sections of (anti-)particles with high precision. However, large systematic uncertainty in measurements of light (anti-)nuclei spectra comes once again from poor knowledge of interaction cross-sections with the detector material.

10

11

12

13

14

15

16

17

18

19

20

21

22

23

24

25

26

27

28

This analysis note describes the measurement of raw primary (anti-)protons and (anti-)deuterons in p–Pb collisions at $\sqrt{s_{NN}} = 5.02 \text{ TeV}$ with the ALICE Experiment. The goal of the analysis is to study the anti-deuteron absorption in ALICE detector material using ratios of raw primary (anti-)deuteron spectra. The same analysis of raw primary (anti-)protons serves as a benchmark for these studies, since the hadronic interaction cross-sections of (anti-)protons are well known from experiment. Event triggering is based on the information from the V0 detector. Charged particle tracks are reconstructed at mid-rapidity ($|\eta| < 0.8$) using the information from central barrel detectors: the Inner Tracking System (ITS) and the Time Projection Chamber (TPC). Specific energy loss in TPC and in ITS and the time-of-flight information from TOF detector are used for (anti-)proton and (anti-)deuteron identification. Raw particle spectra are corrected for amount of secondary particles originating either from weak decays or from spallation processes in detector material. The resulting raw primary antiparticle-to-particle ratios show significant deviations from unity, indicating

29 higher anti-particle interaction cross-sections in the detector material. The ratios are compared to
30 the results from full-scale ALICE simulations using Geant3 and Geant4 toolkits for propagation of
31 (anti-)particles through the ALICE detector. Anti-deuteron inelastic interaction cross-section (aver-
32 aged over the ALICE detector material) is constrained from the comparison between experimental
33 data and Geant4 simulations in the momentum range of $0.5 < p < 4.0 \text{ GeV}/c$.

34 Contents

35	1 Datasets and Event Selection	3
36	1.1 Computing Setup	3
37	1.2 Run Selection	3
38	1.3 Event Selection	3
39	1.4 Monte Carlo Data Samples	4
40	2 Track Selection and Particle Identification	6
41	2.1 Primary Track Selection	6
42	2.2 Particle Identification	6
43	3 Run-by-run QA	10
44	4 Extraction of Raw Primary Spectra	17
45	4.1 Raw Signal Extraction	17
46	4.2 Corrections For Secondary (Anti-)Particles	19
47	4.3 Anti-Particle To Particle Ratios	21
48	5 Systematic Checks and Uncertainties	23
49	5.1 Tracking	23
50	5.2 PID selection	25
51	5.3 Secondary Particles	30
52	5.4 Total systematic uncertainty	30
53	5.5 Global Uncertainty From Primordial Ratio	31
54	6 Ratio of Raw Primary Spectra	33
55	7 Simple Geant4 Model	35
56	8 Constraints on Anti-deuteron Inelastic Cross-section	36
57	9 Plots for Approval	37
58	Appendices	39
59	A Quality Assurance	39
60	A.1 Run-by-run QA	39

61	B TOF mass square fits	44
62	B.1 TOF m^2 fits for (anti-)protons	44
63	B.2 TOF m^2 fits for (anti-)deuterons	50
64	C DCA_{xy} fits	52
65	C.1 DCA _{xy} template fits for (anti-)protons	52
66	C.2 DCA _{xy} fits for (anti-)deuterons	54

67 1 Datasets and Event Selection

68 1.1 Computing Setup

69 For the analysis the following version of ALICE software is used:

70 ROOT::v6-16-00

71 AliRoot::v5-09-47

72 AliPhysics::vAN-20190501

73 The results are obtained with help of analysis code and post-analysis scripts which can be found in the
74 following path:

75 \$ALICE_PHYSICS/PWGFL/NUCLEX/Nuclei/AbsorptionRatios/

76 1.2 Run Selection

77 Proton–lead (p–Pb) collisions recorded in 2016 at a centre-of-mass energy of $\sqrt{s_{\text{NN}}} = 5.02 \text{ TeV}$ are used
78 for this analysis, namely, the data from 2 periods (LHC16q and LHC16t) in AOD format (AOD 190
79 filtering) after pass 1 CENT_wSDD reconstruction. Run list contains only runs for which the global quality
80 status of detectors used in analysis (ITS, TPC, TOF and V0) as well as the physics selection status equal
81 to 1 (i. e. good) in the Run Condition Table (RCT)¹. For both periods the magnetic field polarity in the
82 ALICE central barrel has been set to ++ during data taking.

83 List of good runs selected for the analysis:

84 LHC16q (33 runs):

85 265305, 265308, 265309, 265332, 265334, 265336, 265338, 265339, 265342, 265343, 265344, 265377,
86 265378, 265381, 265383, 265384, 265385, 265387, 265388, 265419, 265420, 265421, 265422, 265424,
87 265425, 265426, 265427, 265435, 265499, 265500, 265501, 265521, 265525

88

89 LHC16t (5 runs):

90 267161, 267163, 267164, 267165, 267166

91

92 Run-by-run trending of event, track and PID variables specific for the current analysis is also investigated.

93 As a result, detector performance is found to be very stable in 16qt periods, and none of the runs has
94 been excluded from the analysis because of strong deviations from value typical for the rest of the runs.

95 More details about this procedure are discussed in Section 3.

96 1.3 Event Selection

97 Minimum bias trigger (kINT7) is used for event selection, which corresponds to simultaneous signal in
98 two V0 scintillators covering the pseudorapidity ranges $2.8 < \eta < 5.1$ (V0A) and $-3.7 < \eta < -1.7$
99 (V0C). Events are required to pass the physics selection with an additional background rejection turned
100 on as recommended by the Data Preparation Group². Several criteria based on the information from the
101 V0 and SPD detectors are applied to each collision in order to make sure that out-of-bunch pile-up and
102 other background events (such as beam-gas interactions or collisions with debunched protons) do not
103 pass the physics selection. For primary vertex the following requirements are applied:

- 104 – Vertex position within $\pm 10 \text{ cm}$ from the geometrical centre of the detector along beam axis
- 105 – At least 1 track/tracklet contributing to vertex reconstruction

¹<https://alimonitor.cern.ch/configuration/>

²<https://twiki.cern.ch/twiki/bin/viewauth/ALICE/AliDPGtoolsEventProp>.

- 106 – Rejection of SPD vertices for which only z coordinate is reconstructed and it is determined with
- 107 poor resolution (defined as the square root of vertex covariance matrix element “ZZ”, with max.
- 108 resolution = 0.25 cm)
- 109 – Cut on absolute distance between vertices reconstructed with tracks and with SPD tracklets (with
- 110 max. displacement = 0.5 cm)

111 Distribution of SPD vertex resolution and correlation between SPD and track vertex positions can be seen
 112 in Fig. 1. Figure shows minimum bias events from LHC16qt periods after physics selection and other
 113 vertex requirements, but the corresponding vertex cuts on resolution and displacement are not applied.
 114 These cuts further remove only 0.8% of all events.

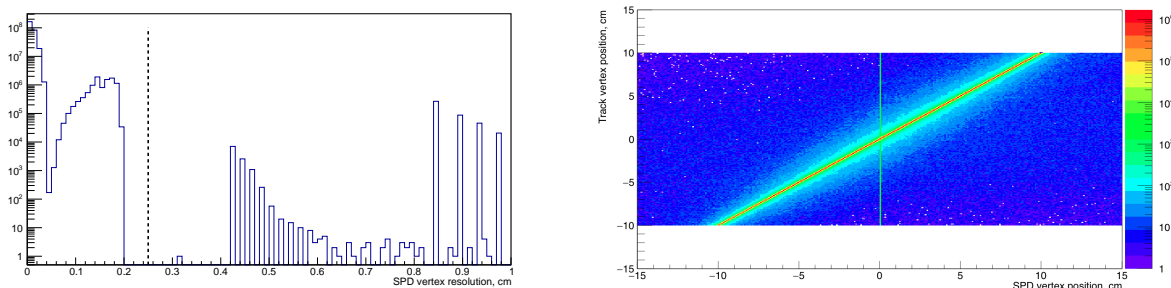


Fig. 1: SPD vertex resolution (left) and correlation between SPD and track vertex Z positions (right) for minimum bias events in LHC16qt periods after physics selection and other vertex requirements (vertex cuts on resolution and displacement are not applied). The corresponding cut on vertex resolution used in analysis is shown as vertical dashed line on the left plot.

- 115 To make sure that all detectors used in track reconstruction cover the central pseudorapidity region of
 116 $|\eta| < 0.8$ with uniform acceptance, vertex position is required to be within ± 10 cm from the geometrical
 117 centre of the detector along beam axis (Fig. 2), with $\sim 13\%$ of all events lying outside of these limits.
 118 In total $N_{MB} = 302.82 \times 10^6$ minimum bias events are selected for further analysis on single track level
 119 (263.77 $\times 10^6$ events from LHC16q period and 39.05 $\times 10^6$ events from LHC16t).

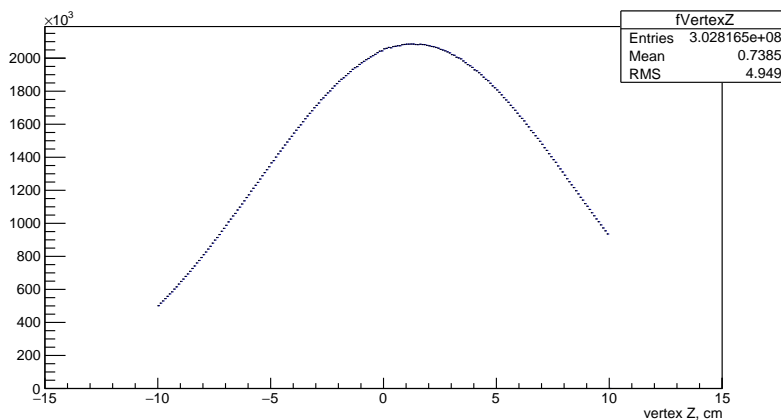


Fig. 2: Distribution of vertex Z position in events selected for the analysis.

120 1.4 Monte Carlo Data Samples

- 121 In this analysis Monte Carlo simulated data are not used directly for the studies of detector inefficiency
 122 and corresponding correction of raw primary (anti-)proton and (anti-)deuteron spectra. The Monte Carlo
 123 samples listed in the Table 1 are used instead to investigate the difference between antiparticle-to-particle
 124 ratios obtained with Geant3 and Geant4 toolkits for propagation through the detector. They are also used

125 to obtain DCA templates of primary/secondary particles needed for the correction of raw (anti-)particle
 126 spectra for amount of secondary particles (Section 4.2) and to evaluate the systematic uncertainties due
 127 to track and PID selection (Section 5). Every MC production is anchored to the corresponding data
 128 taking period in the sense that one tries to reproduce in all details detector configuration extracted from
 129 the Offline Conditions DataBase (OCDB) in the simulation, including active ITS zones and dead pixels,
 130 voltage settings, noisy channels and other detector-specific effects. For the analysis of general-purpose
 131 Monte Carlo data, the same list of runs is used as in experimental data analysis (MC productions with
 132 injected nuclei are anchored to run number 265525).

Table 1: Monte Carlo simulated data used in analysis

MC production	Type	Geant version	Generator	Link to JIRA ticket
LHC17f2b	General-purpose	Geant3	DMPJET	7100
LHC18f3	General-purpose	Geant3	DMPJET	7792
LHC19b1	Nuclei injected	Geant4	Nuclei Box	8197
LHC19b1b	Nuclei injected	Geant3	Nuclei Box	8197

133 2 Track Selection and Particle Identification

134 2.1 Primary Track Selection

135 In order to select well reconstructed physical tracks originating from primary event vertex and suppress
 136 secondary tracks from weak decays or spallation processes in detector material, the following track cuts
 137 are applied:

Table 2: AOD track cuts used in analysis

Variable	Requirement
p	$> 0.2 \text{ GeV}/c$
$ \eta $	< 0.8
AOD FilterBit	256
Number of ITS clusters	≥ 2
$ \text{DCA}_{xy} $	$< 0.1 \text{ cm}$
$ \text{DCA}_z $	$< 0.2 \text{ cm}$

138 The AOD FilterBit 256 includes several requirements for a track to have a certain reconstruction quality
 139 in the TPC and ITS detectors, including the requirement of a hit in one of the two layers of SPD detector.
 140 Cuts on the distance of closest approach (DCA) to the event vertex are chosen to be relatively tight in
 141 order to suppress secondary (anti-)particles originating from e.g. weak decays such as $\Lambda \rightarrow p\pi^-$ with a
 142 $c\tau \sim 7.89 \text{ cm}$. The resulting distributions of cut variables are shown in Fig. 3 for (anti-)protons and in
 143 Fig. 4 for (anti-)deuterons.

144 2.2 Particle Identification

145 (Anti-)protons and (anti-)deuterons are identified in this analysis via their specific energy loss in the
 146 TPC as well as with time-of-flight information from the TOF detector. For (anti-)deuteron analysis,
 147 additional selection based on ITS PID information is applied to all tracks below $p = 1.4 \text{ GeV}/c$. Usage
 148 of supplementary information from different detectors allows one to reduce the fraction of mis-identified
 149 hadrons in final sample to a minimum, while preserving a high efficiency for selection of (anti-)particles
 150 of interest. The detector's PID response is expressed in terms of deviations between measured and
 151 expected values for a given species hypothesis and particle momentum, normalised by detector PID
 152 resolution (σ). For example, TPC PID information for proton hypothesis is given in units of $\text{TPCn}\sigma_p$
 153 defined as following:

$$\text{TPCn}\sigma_p = \frac{(\text{d}E/\text{d}x)_{\text{measured}} - \langle \text{d}E/\text{d}x(p) \rangle_{\text{expected}}}{\sigma_p}. \quad (1)$$

154 PID selection criteria used in the analysis are listed below, and all requirements described in this section
 155 are the same between the corresponding particles and antiparticles:

156 Below $p = 0.7 \text{ GeV}/c$ ($p = 1.4 \text{ GeV}/c$), protons (deuterons) can be identified via their specific energy
 157 loss in the TPC detector. In addition to TPC PID selection criteria, at low momentum (anti-)deuterons
 158 are required to have $\text{ITSn}\sigma_d > -2.0$; more details about this PID selection are discussed in Section 5.2.
 159 Above $p = 2.5 \text{ GeV}/c$ ($p = 1.4 \text{ GeV}/c$), proton and deuteron candidates are required to have an associated
 160 hit in the TOF detector, and their yield is extracted using fit to TOF m^2 distribution as described in
 161 Section 4.1. In the momentum range $0.7 < p < 2.5 \text{ GeV}/c$, protons are required to fulfil $|\text{TOFn}\sigma_p| < 3.0$
 162 selection, since the fit to TOF m^2 distribution doesn't describe the experimental data in all details (see
 163 Section 4.1 for further discussions).

164 The resulting TPC and TOF PID signal as a function of track momentum p are shown for proton and
 165 deuteron candidates in Fig. 5.

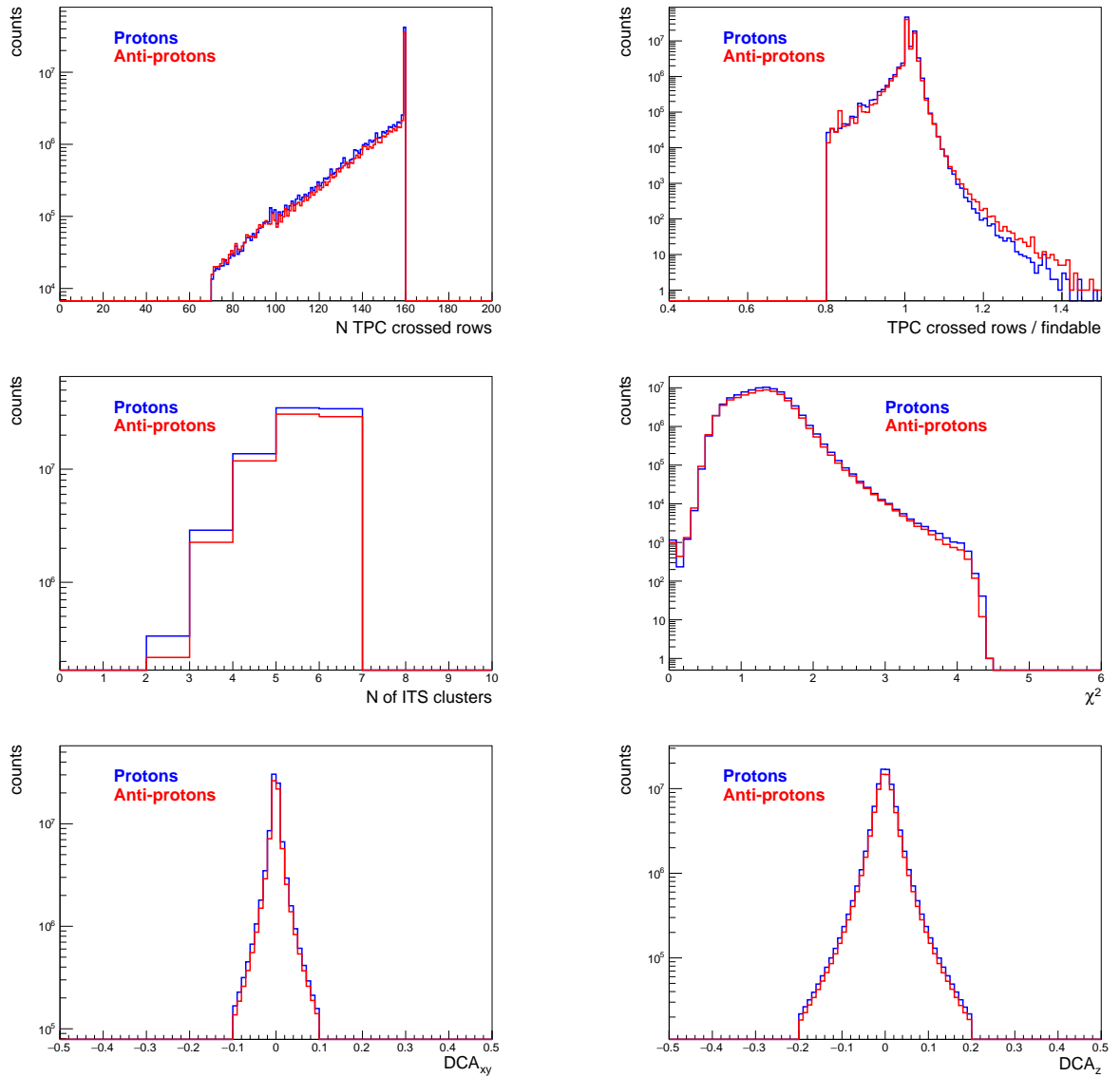


Fig. 3: Distribution of various tracking parameters after track selection listed in Table 2 for protons (red) and anti-protons (blue).

166 Usage of information from the TOF detector implies that a track has to penetrate the Transition Radiation
 167 Detector (TRD) located between the TPC and TOF detectors. With radiation length of $X_0 \sim 24.7\%$ [1],
 168 TRD has a significant impact on raw primary antiproton-to-particle ratios as discussed in Section 6.

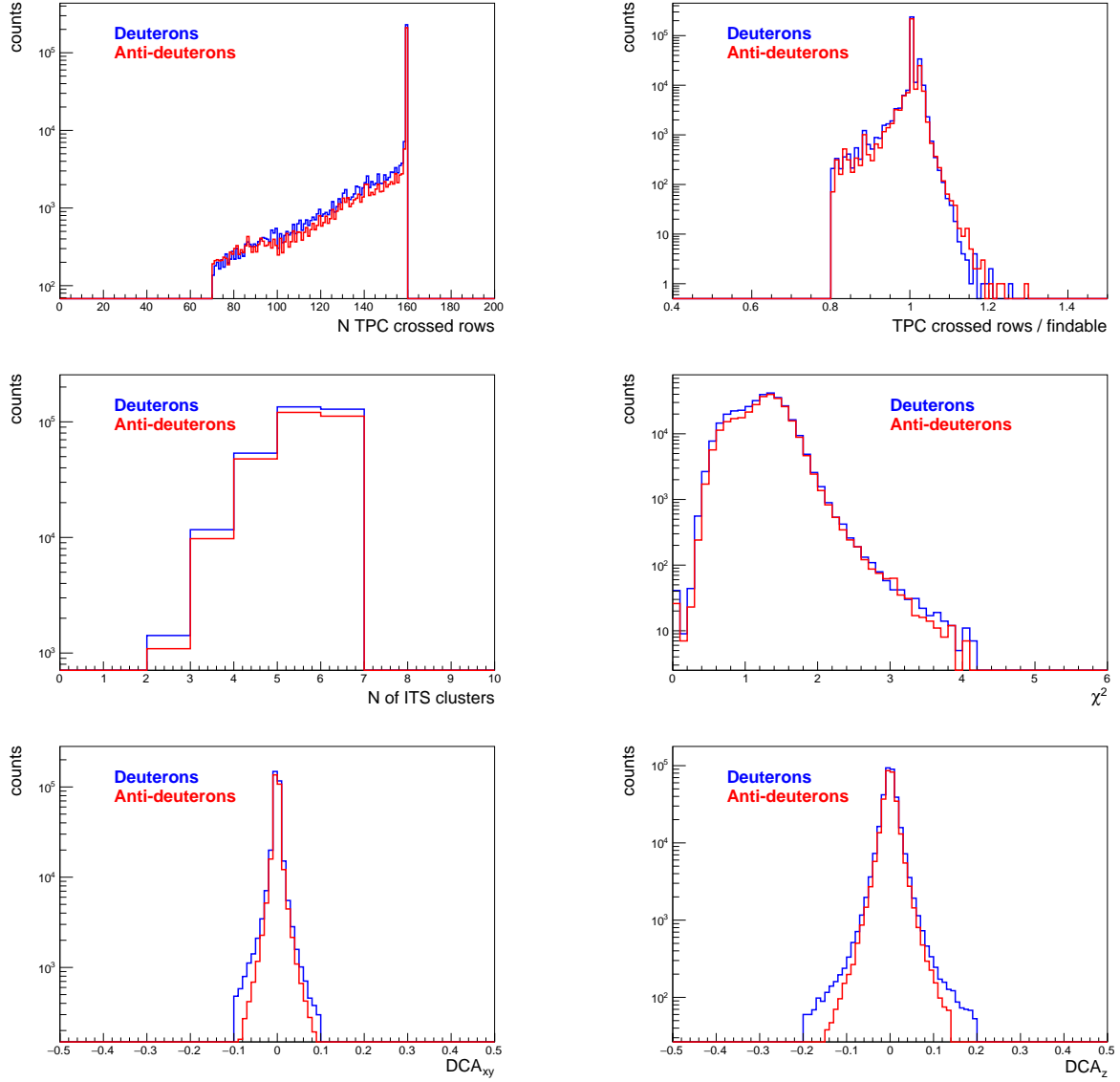


Fig. 4: Distribution of various tracking parameters after track selection listed in Table 2 for deuterons (red) and anti-deuterons (blue).

Table 3: PID selection used in analysis

Detector	Particle	Requirement	Momentum range [GeV/c]
TPC (dE/dx)	proton	$ TPCn\sigma_p < 3.0$	$[0.2, \infty]$
	proton	$ TOFn\sigma_p < 3.0$	$[0.7, 2.5]$
	proton	Matched hit	$[2.5, \infty]$
TOF (β)	deuteron	$ TPCn\sigma_d < 3.0$	$[0.2, \infty]$
	deuteron	$ITSn\sigma_d > -2.0$	$[0.2, 1.4]$
	deuteron	Matched hit	$[1.4, \infty]$

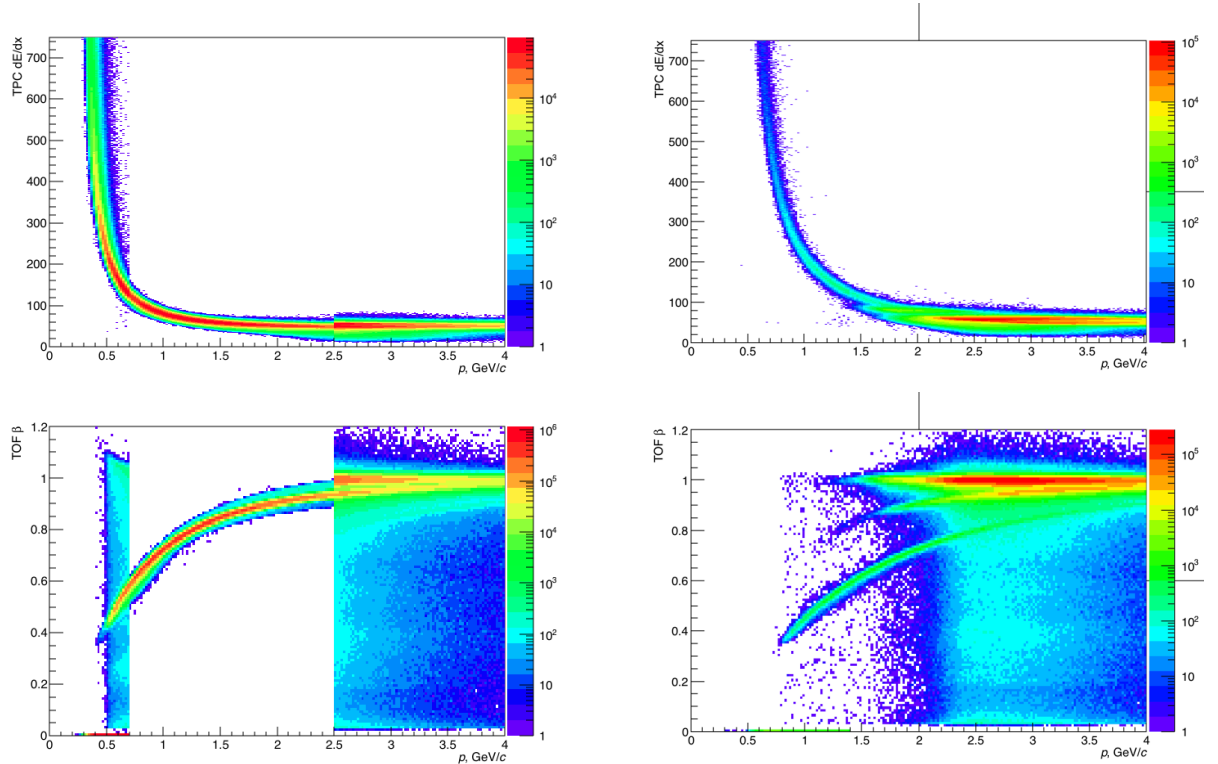


Fig. 5: TPC dE/dx (top row) and TOF β (bottom row) for proton (left) and deuteron (right) candidates as a function of track momentum p after PID selection listed in Table 3. In momentum range $p > 2.5 \text{ GeV}/c$ ($p > 1.4 \text{ GeV}/c$) the yield of protons (deuterons) and their anti-particles is extracted from fit to TOF m^2 distribution (Section 4.1).

169 3 Run-by-run QA

170 Several checks based on detector performance, track matching, calibration etc. are performed for all
 171 reconstructed data by the ALICE Quality Assurance group in a centralised way. The results of such
 172 checks are displayed in RCT as quality flags for each detector and each run. Only good runs are used
 173 in this analysis, with a detector status of 1 for ITS, TPC, TOF and V0 detectors as well as good physics
 174 selection status 1.

175 On top of these selections additional run-by-run checks are performed for all variables relevant for the
 176 analysis on event, track and PID level in experimental data. Since some conditions of data taking could
 177 be non-stable as a function of time, even a good (according to RCT) run can differ from the rest of the
 178 period in terms of relevant values and bias final results. To check the stability of detector performance,
 179 mean values of event, track and pair variables are extracted for each run, and corresponding trends are
 180 analysed as a function of time (run number). As a result, detector performance is found to be stable
 181 during 2016 p–Pb data taking period, and none of the runs have been further excluded from the final
 182 analysis due to large deviations of relevant variables from the rest of the period. Moreover, all trends
 183 have been found to be very similar between particles and antiparticles, which indicates that any possible
 184 run-by-run variations in detector performance have negligible impact on the final ratios of raw primary
 185 spectra.

186 For all checks described in this Section (anti-)proton and (anti-)deuteron candidates are selected with the
 187 same track and PID cuts as described in Section 2.2, but with an additional strict TOF PID requirement at
 188 high momentum (Table 4). As can be seen from Fig. 6, this minimises the impact of large contamination
 189 at high momentum in comparison with Fig. 5 where only matched TOF hit is required.

Table 4: PID selection used for run-by-run QA checks

Detector	Particle	Requirement	Momentum range [GeV/c]
TPC (dE/dx)	proton	$ TPCn\sigma_p < 3.0$	$[0.2, \infty]$
TOF (β)	proton	$ TOFn\sigma_p < 3.0$	$[0.7, \infty]$
TPC (dE/dx)	deuteron	$ TPCn\sigma_d < 3.0$	$[0.2, \infty]$
ITS (dE/dx)	deuteron	$ITSn\sigma_d > -2.0$	$[0.2, 1.4]$
TOF (β)	deuteron	$ TOFn\sigma_d < 3.0$	$[1.4, \infty]$

190 The resulting mean number of (anti-)proton and (anti-)deuteron candidates per event after such PID
 191 selection is shown in Figs. 7 and 8 as a function of run number for momentum-integrated tracks. As in
 192 other plots in this Section, horizontal lines indicate the median value of all points across all runs (central
 193 line) and ± 3 times the RMS value of spread around median (upper and lower lines); vertical dashed
 194 line corresponds to the border between LHC16q and LHC16t data taking periods. As can be seen from
 195 Figs. 7 and 8, mean number of (anti-)proton and (anti-)deuteron candidates per event stays stable as a
 196 function of time, with all data points being within ± 3 RMS of spread from the median value across all
 197 runs.

198 For (anti-)proton and (anti-)deuteron candidates selected in this way, following tracking and PID parameters
 199 (mean values) are controlled as a function of run number:

- 200 – DCA_{xy} and DCA_z
- 201 – Number of TPC clusters and TPC crossed rows, ratio TPC crossed rows / findable TPC clusters
 and fraction of shared TPC clusters
- 202 – Number of ITS clusters
- 203 – TPC χ^2 value
- 204 – TPC and TOF $n\sigma_{p,d}$
- 205 – $ITSn\sigma_d$

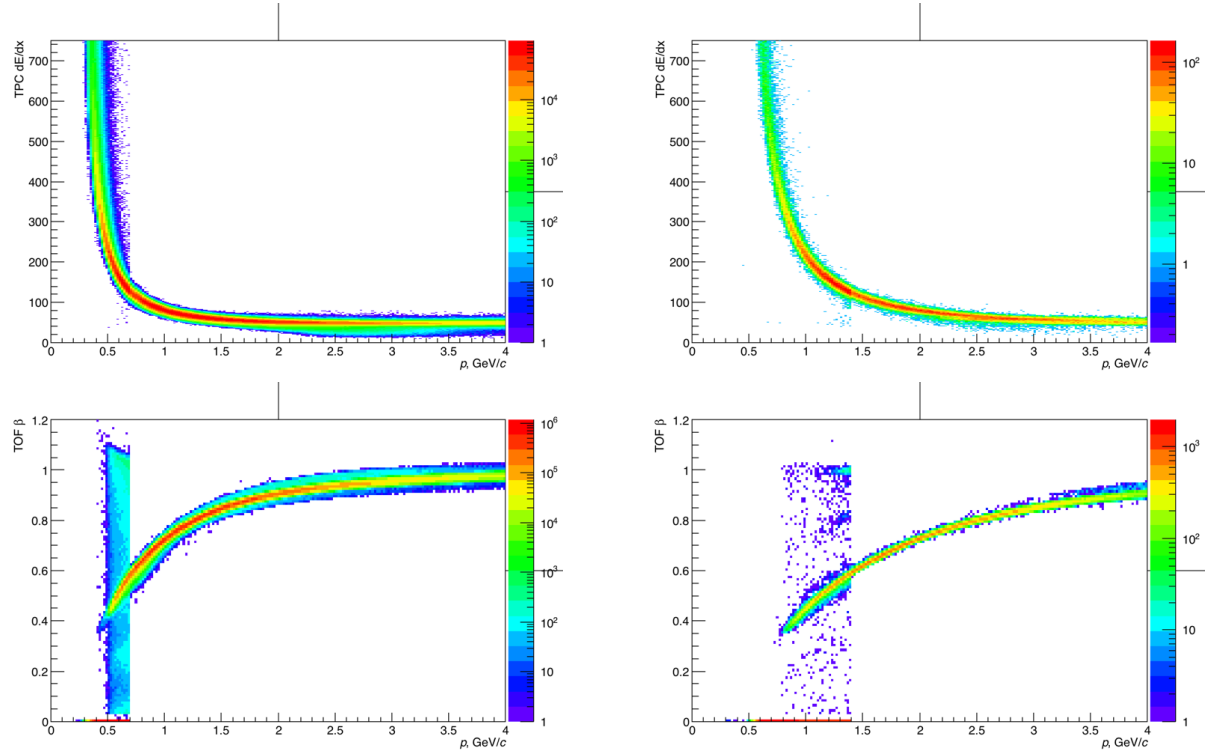


Fig. 6: TPC dE/dx (top row) and TOF β (bottom row) for proton (left) and deuteron (right) candidates as a function of track momentum p after the PID selection listed in Table 4.

207 Some variables, as anticipated, are found to be highly correlated, e. g. number of TPC clusters, TPC
 208 crossed rows and ratio crossed rows / findable clusters. All trends are found to be very similar between
 209 particle and anti-particle candidates. Figures in the current Section show the results for momentum-
 210 integrated (anti-)proton candidates, and corresponding plots for (anti-)deuteron candidates can be found
 211 in Appendix A.

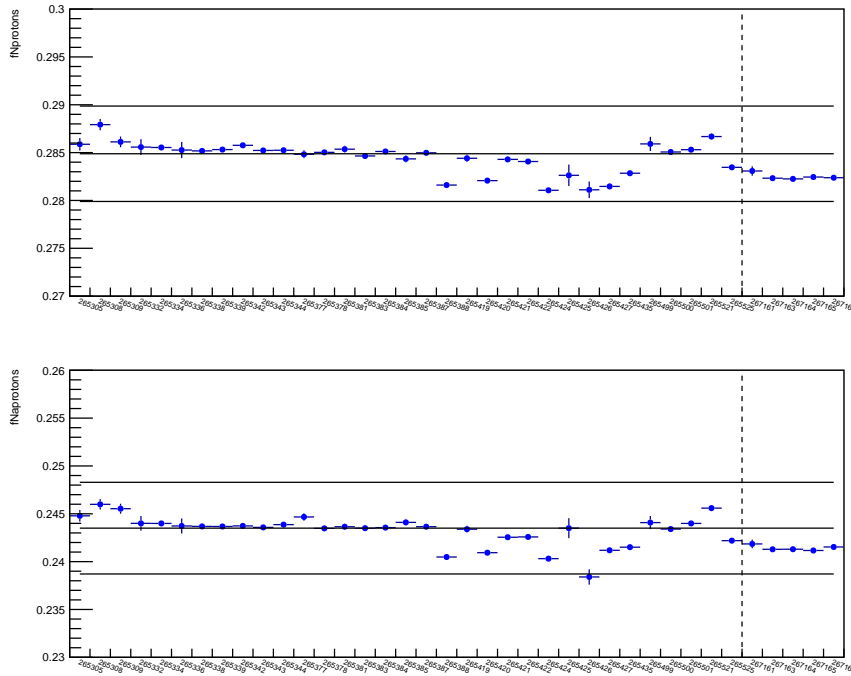


Fig. 7: Mean number of proton (top) and anti-proton (bottom) candidates per event after PID selection listed in Table 4 as a function of run number.

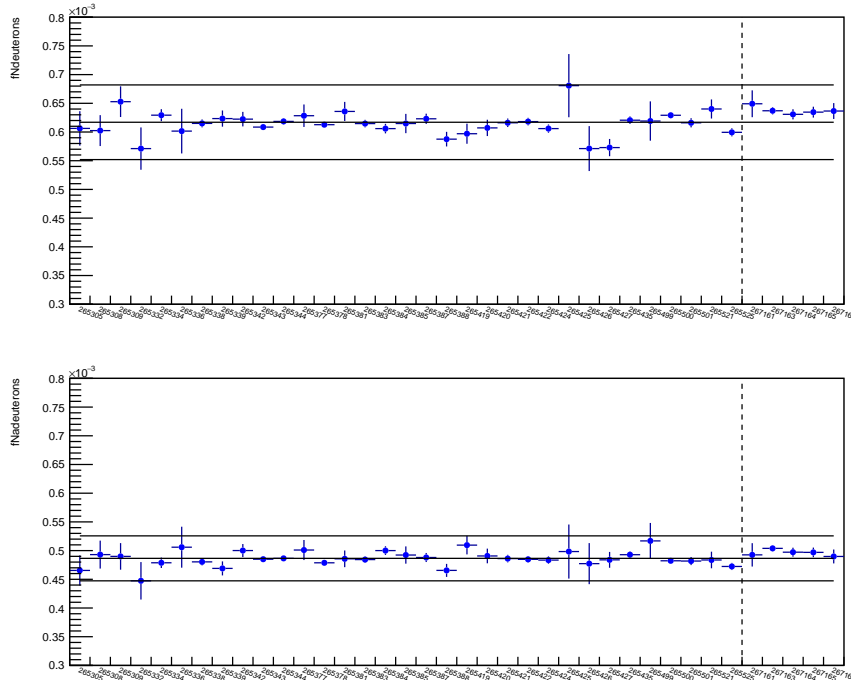


Fig. 8: Mean number of deuteron (top) and anti-deuteron (bottom) candidates per event after PID selection listed in Table 4 as a function of run number.

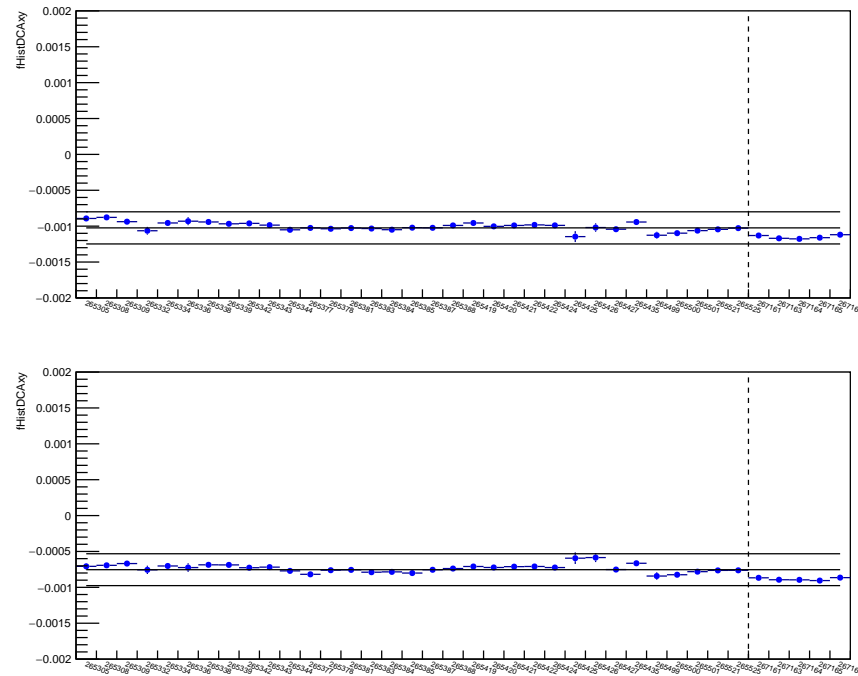


Fig. 9: Mean DCA_{xy} for proton (top) and anti-proton (bottom) candidates as a function of run number.

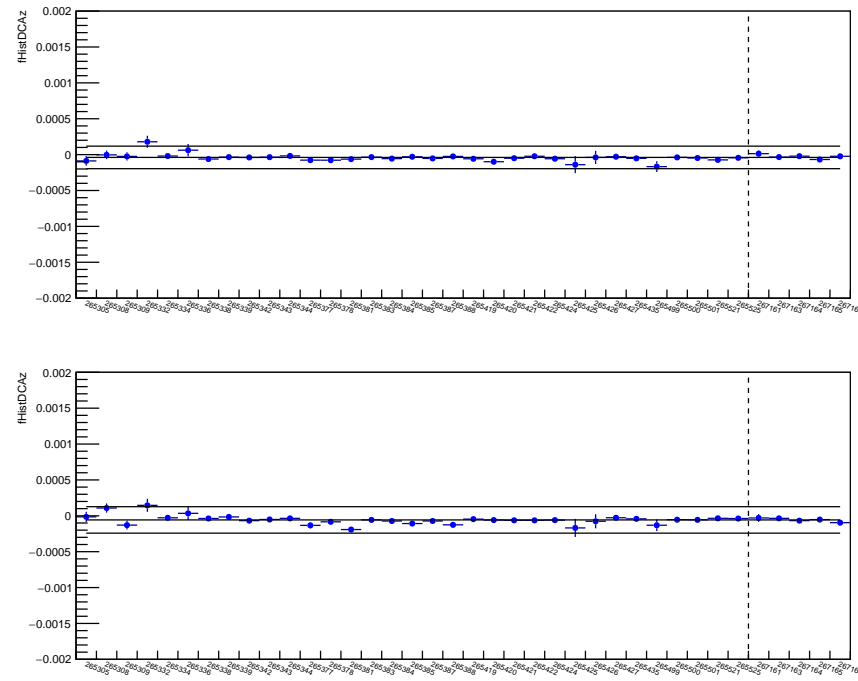


Fig. 10: Mean DCA_z for proton (top) and anti-proton (bottom) candidates as a function of run number.

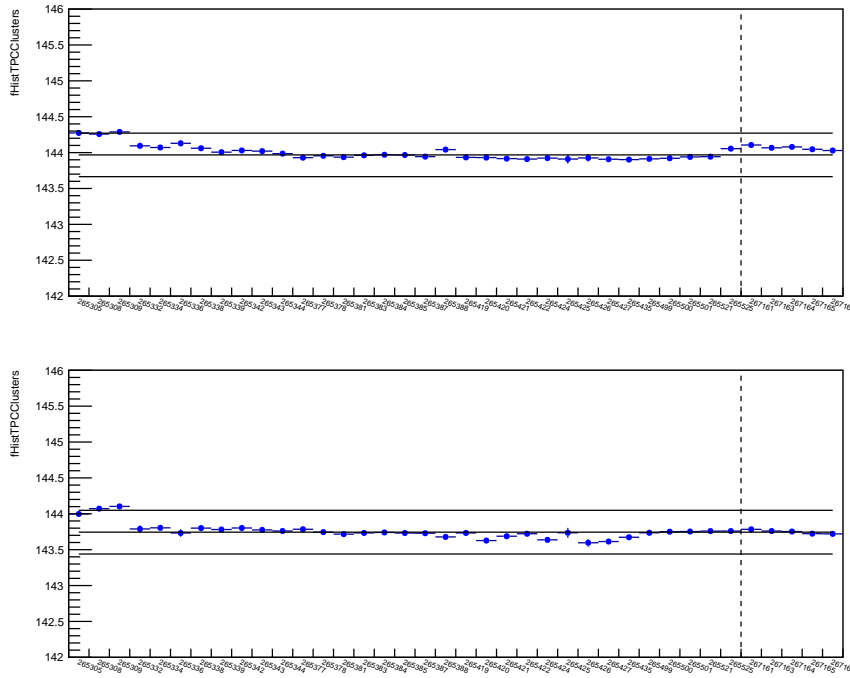


Fig. 11: Mean number of TPC clusters for proton (top) and anti-proton (bottom) candidates as a function of run number.

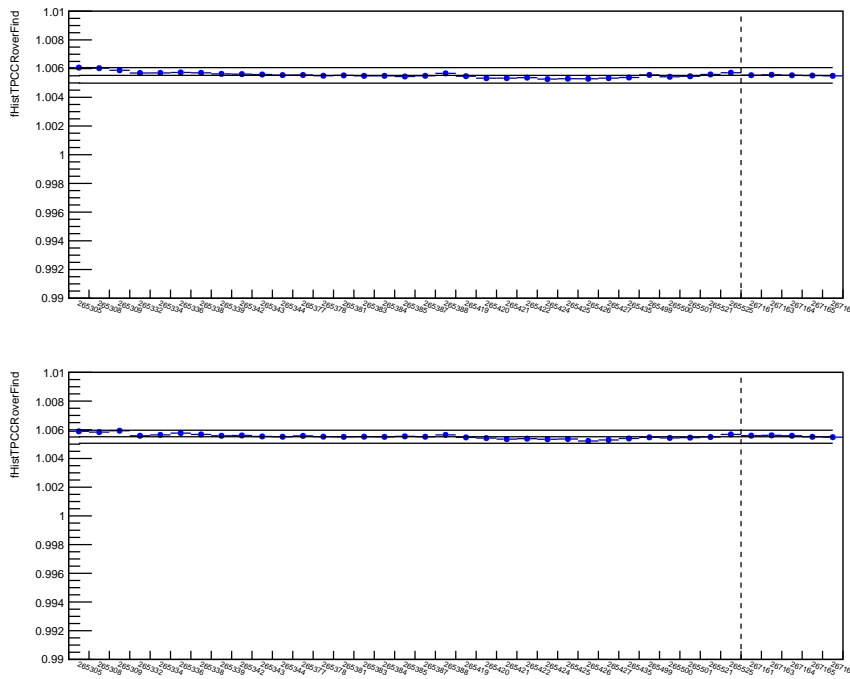


Fig. 12: Mean ratio of TPC crossed rows over findable clusters for proton (top) and anti-proton (bottom) candidates as a function of run number.

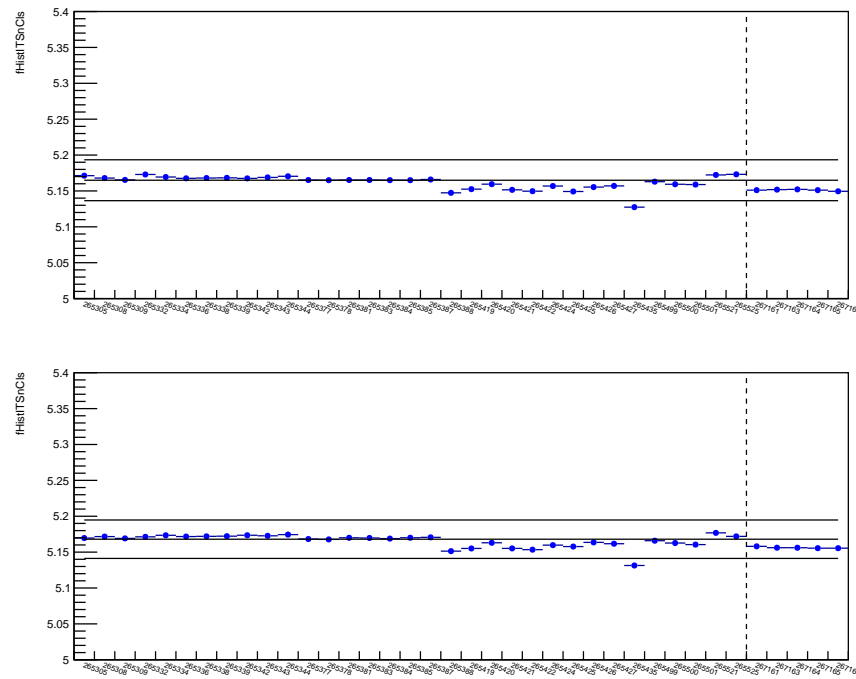


Fig. 13: Mean number of ITS clusters for proton (top) and anti-proton (bottom) candidates as a function of run number.

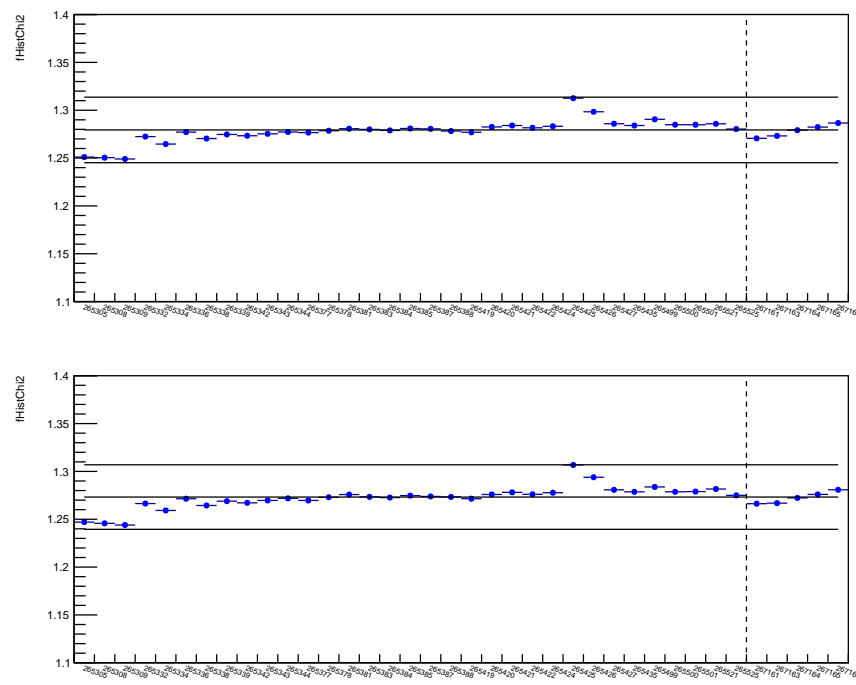


Fig. 14: Mean TPC χ^2 value for proton (top) and anti-proton (bottom) candidates as a function of run number.

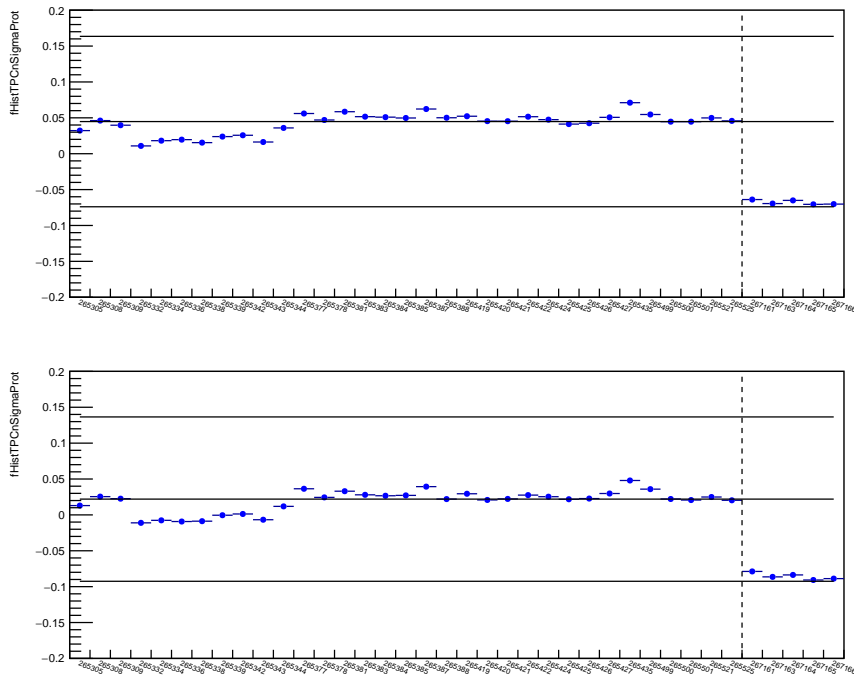


Fig. 15: Mean $\text{TPC}n\sigma_p$ for proton (top) and anti-proton (bottom) candidates as a function of run number.

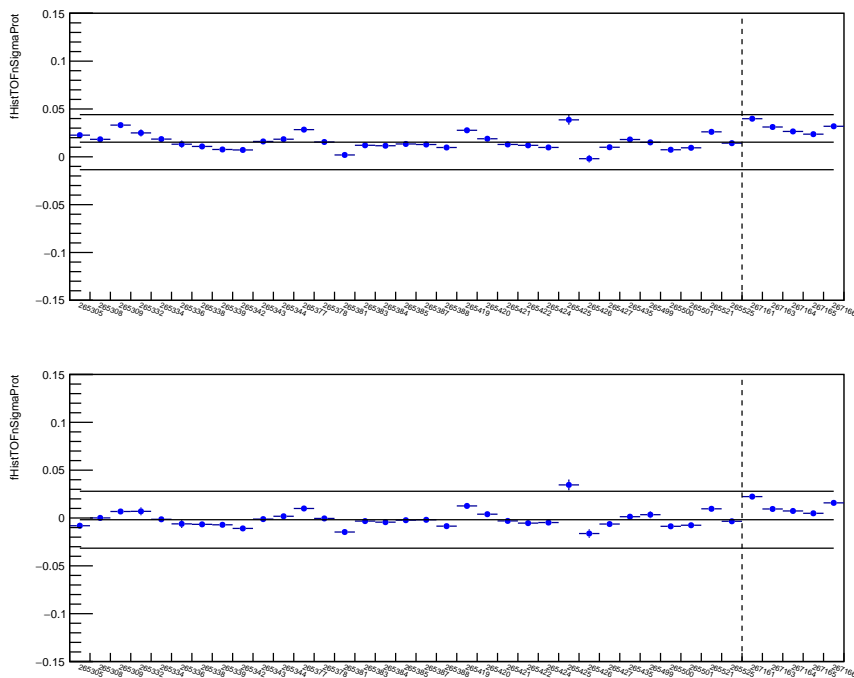


Fig. 16: Mean $\text{TOF}n\sigma_p$ for proton (top) and anti-proton (bottom) candidates as a function of run number.

212 **4 Extraction of Raw Primary Spectra**

213 **4.1 Raw Signal Extraction**

214 This Section describes the procedure used to extract raw spectra of (anti-)protons and (anti-)deuterons.
 215 The analysis can be divided into several momentum ranges according to PID selection (Table 3); for
 216 (anti-)protons these ranges are:

- 217 – $0.3 < p < 0.7 \text{ GeV}/c$: raw yield is extracted as counts of (anti-)protons after PID selection (using
 218 PID information from the TPC detector only)
- 219 – $0.7 < p < 2.5 \text{ GeV}/c$: raw yield is extracted as counts of (anti-)protons after PID selection (using
 220 PID information from the TPC and TOF detectors); raw spectra are corrected for the purity of
 221 (anti-)proton sample in this momentum range as described below
- 222 – $2.5 < p < 4.0 \text{ GeV}/c$: tracks are required to have a matched TOF hit, and raw (anti-)proton yield
 223 is extracted with fits to TOF m^2 distributions as described below

224 For (anti-)deuteron analysis, these ranges can be summarised as following:

- 225 – $0.5 < p < 1.4 \text{ GeV}/c$: raw yield is extracted as counts of (anti-)deuterons after PID selection (using
 226 PID information from the ITS and TPC detectors)
- 227 – $1.4 < p < 4.0 \text{ GeV}/c$: tracks are required to have a matched TOF hit, and raw (anti-)deuteron yield
 228 is extracted with fits to TOF m^2 distributions as described below

229 With time of flight t of a track provided by the TOF detector, the particle's mass square can be calculated
 230 as:

$$m^2 = \frac{p^2}{c^2} \left(\frac{c^2 t^2}{L^2} - 1 \right), \quad (2)$$

231 where p and L are the track's momentum and length correspondingly. Fig. 17 shows TOF m^2 as a function
 232 of particle's momentum for proton and deuteron candidates after PID selection according to Table 3.

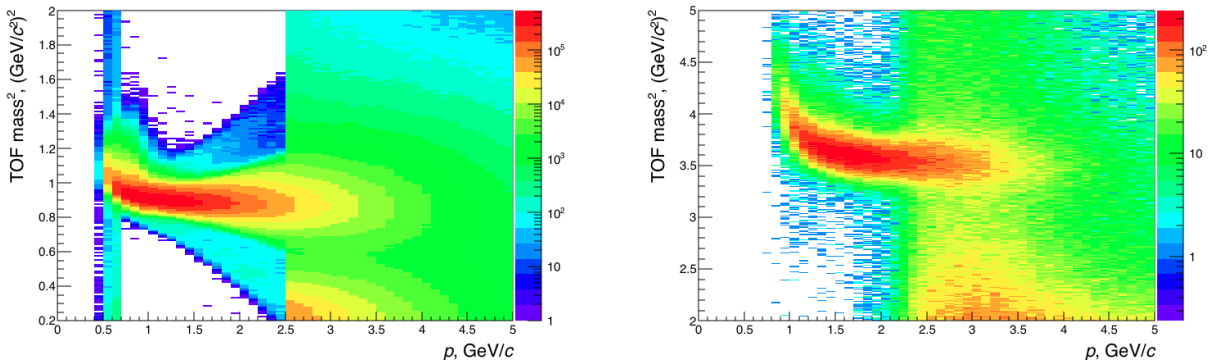


Fig. 17: TOF mass square m^2 as a function of particle's momentum p for proton (left) and deuteron (right) candidates after PID selection. In momentum range $p > 2.5 \text{ GeV}/c$ ($p > 1.4 \text{ GeV}/c$), raw proton (deuteron) yield is extracted with fits to TOF m^2 distributions.

233 Following the approach described in [2], signal peak (both for (anti-)protons and for (anti-)deuterons)
 234 is parametrised with the function $s(m^2) = I\hat{s}(m^2)$, where I is integral of the function and $\hat{s}(m^2)$ is the
 235 corresponding normalised function defined as [2]:

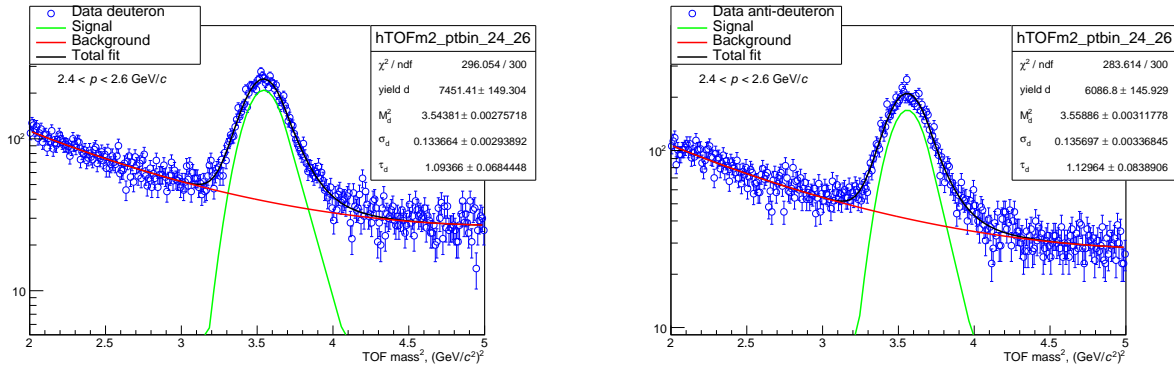


Fig. 18: Fit to TOF mass square distribution in momentum bin $2.4 < p < 2.6 \text{ GeV}/c$ for deuteron (left) and anti-deuteron (right) candidates.

$$\hat{s}(m^2) = \begin{cases} c_0 \exp\left[-\frac{(m^2 - \mu)^2}{2\sigma^2}\right], & m^2 \leq \mu + \tau\sigma \\ c_0 \exp\left[-(m^2 - \mu - \frac{\tau}{2}\sigma)\frac{\tau}{\sigma}\right], & m^2 > \mu + \tau\sigma \end{cases} \quad (3)$$

236 Here μ and σ correspond to signal mean and width values, and τ is a parameter needed to describe
237 exponential tail of TOF response. The normalisation parameter c_0 is given by [2]:

$$c_0 = \frac{1}{\sqrt{\frac{\pi}{2}} \left[\sigma + \sigma \operatorname{erf}\left(\frac{\tau}{\sqrt{2}}\right) \right] + \frac{\sigma}{\tau} e^{-\tau^2/2}}. \quad (4)$$

238 Once $\hat{s}(m^2)$ function is properly normalised, both (anti-)particle yield and statistical error are returned
239 directly by the fit. The background $b(m^2)$, originating mainly from tracks with mis-matched TOF hit or
240 from tail of lower mass particles, is parametrised with the following function:

$$b(m^2) \sim \exp(p_0 + p_1 m^2 + p_2 m^4). \quad (5)$$

241 This approach is used for (anti-)deuterons in all analysed momentum bins above $p = 1.4 \text{ GeV}/c$. An
242 example of fit to TOF m^2 distributions of deuterons and anti-deuterons is shown in Fig. 18, and fits in all
243 momentum bins can be found in Appendix B.

244 For (anti-)protons, an additional function for kaon peak (according to Eq. 3) is added to background,
245 which is visible at $m^2 \sim 0.25 \text{ GeV}/c^2$ (Fig. 19). The resulting fit function describes confidently (anti-
246)proton TOF m^2 distributions above $p = 2.5 \text{ GeV}/c$, fits in all momentum bins can be found in Ap-
247 pendix B.

248 Below $p = 2.5 \text{ GeV}/c$, the signal function cease to describe (anti-)proton peak in all details, with dis-
249 agreement becoming worse in lower momentum bins. It is worth to note that a peculiar shape of (anti-)
250 proton peak at very low momentum seems to be reproduced (at least qualitatively) by Monte Carlo
251 simulations, with a shoulder of (yet) unknown origin in anti-proton distribution at lower mass (Fig. 20).
252 Therefore, in the momentum range $0.7 < p < 2.5 \text{ GeV}/c$ raw (anti-)proton yield is extracted after PID
253 selection of $|\text{TOFn}\sigma_p| < 3.0$, which also cuts away aforementioned shoulder in TOF m^2 distribution. The
254 purity of (anti-)proton sample in this momentum region is estimated with TOF m^2 distributions without
255 $|\text{TOFn}\sigma_p| < 3.0$ selection (only requiring matched TOF hit). The distributions are fitted with background

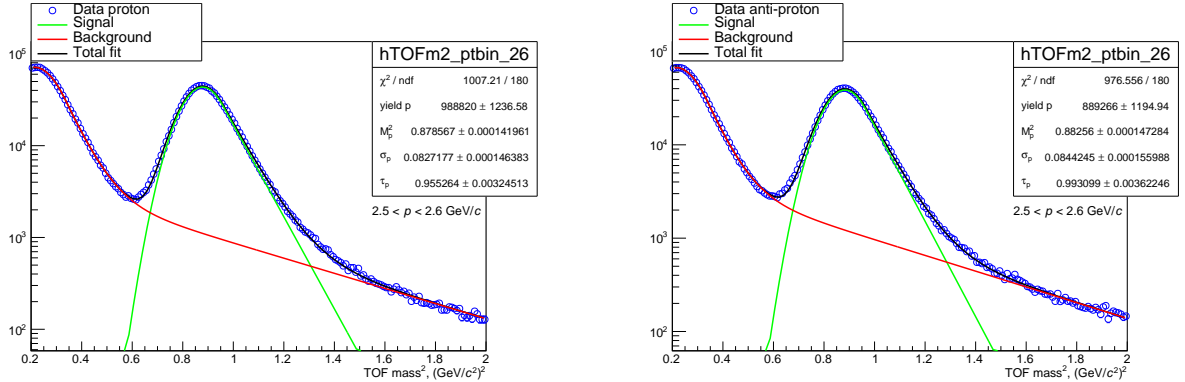


Fig. 19: Fit to TOF mass square m^2 distribution in momentum bin $2.5 < p < 2.6 \text{ GeV}/c$ for proton (left) and anti-proton (right) candidates.

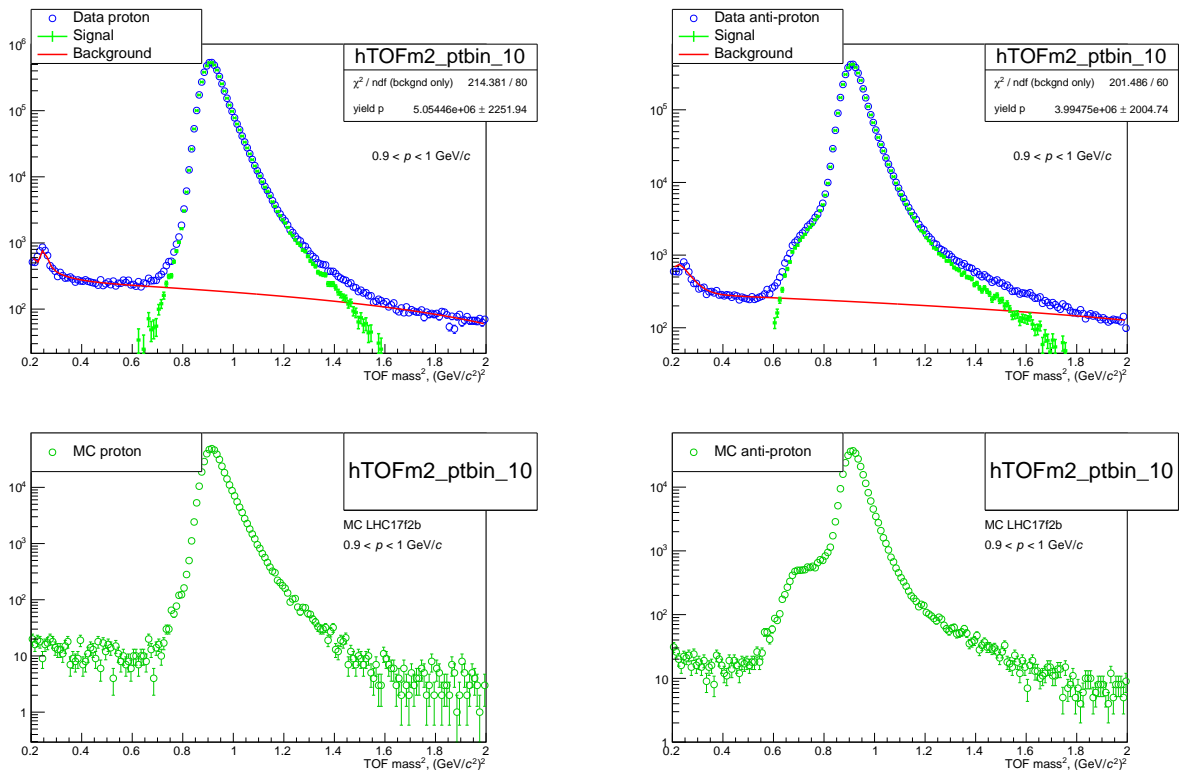


Fig. 20: Top row: fit to TOF mass square m^2 distribution in momentum bin $0.9 < p < 1.0 \text{ GeV}/c$ for proton (left) and anti-proton (right) candidates in experimental data. Fit is performed by using only background function in TOF m^2 regions $(0.2, 0.6)$ and $(1.8, 2.0)(\text{GeV}/c)^2$. Bottom row: TOF mass square distribution in the same momentum bin for pure primary protons (left) and anti-protons (right) in Monte Carlo simulations (LHC17f2b).

function outside of peak region (Fig. 20 top row), and the purity is evaluated in $\pm 3\sigma$ range around signal peak. The resulting (anti-)proton purity is shown in Fig. 21 as a function of momentum and is applied to raw (anti-)proton counts after $|\text{TOFn}\sigma_p| < 3.0$ selection.

The resulting raw (anti-)particle spectra are shown in Fig. 22.

4.2 Corrections For Secondary (Anti-)Particles

Raw spectra shown in Fig. 22 need to be corrected for the amount of secondary (anti-)particles survived track cuts and PID selection. To this purpose, the DCA distributions in transverse plane to the beam direction (DCA_{xy}) are analysed as a function of track's momentum p . Such distributions are different for

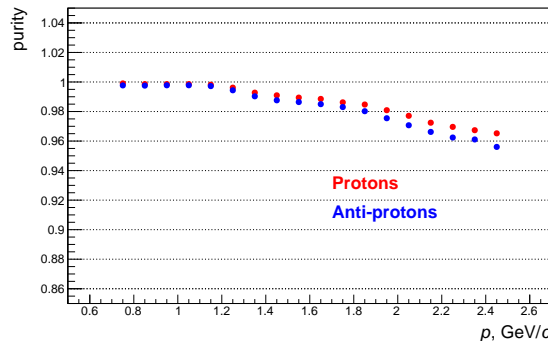


Fig. 21: Purity of (anti-)proton sample after $|TOFn\sigma_p| < 3.0$ selection as a function of momentum.

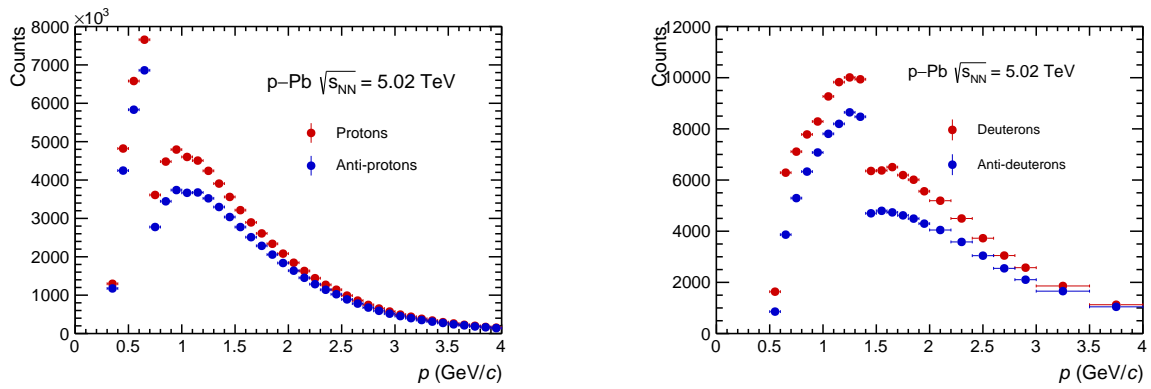


Fig. 22: Raw (anti-)proton (left) and (anti-)deuteron (right) spectra. Corrections for secondary (anti-)particles are not applied.

264 primary tracks and for secondary (anti-)particles originating from weak decays or spallation processes in
265 detector material.

266 For (anti-)proton analysis, the corresponding shapes of DCA_{xy} distributions are taken from general-
267 purpose Monte Carlo production LHC17f2b. Experimental data are fitted with 3 components (primaries,
268 secondaries from material and secondaries from weak decays) in different momentum bins using the
269 `TFractionFitter` class of ROOT. In order to allow for more reliable fit, DCA_{xy} cut is relaxed to
270 $|DCA_{xy}| < 1.0\text{cm}$ (both in MC and in experimental data analysis), and the fraction of primary (anti-)
271 protons is extracted as ratio of primary (anti-)protons over sum in $|DCA_{xy}| < 0.1\text{cm}$. Fig. 23 shows
272 an example of such template fit in momentum bin $0.6 < p < 0.7\text{GeV}/c$, the results in all momentum
273 bins can be found in Appendix C. Because of relatively tight tracking requirements used in the analysis
274 (Table 2), resulting purity of (anti-)proton sample stays high in all investigated momentum bins, with an
275 anti-proton purity being slightly higher at low momentum (Fig. 24). These results have been found to be
276 in qualitative agreement with the predictions from general-purpose Monte Carlo simulations, which are
277 also shown in the same Figure.

278 In (anti-)deuteron analysis correction for secondary particles is applied only for deuteron candidates, and
279 the fraction of secondary anti-deuterons is assumed to be zero. Similar procedure is used to fit deuteron
280 DCA_{xy} distributions in momentum bins using sum of 2 components (primaries and secondaries from
281 material). Experimental anti-deuteron data is used in each bin as a template for signal, and the shape of
282 secondary deuterons is taken from general-purpose Monte Carlo simulations (LHC17f2b and LHC18f3).
283 Resulting purity of deuteron sample as a function of track momentum is shown in Fig. 26.

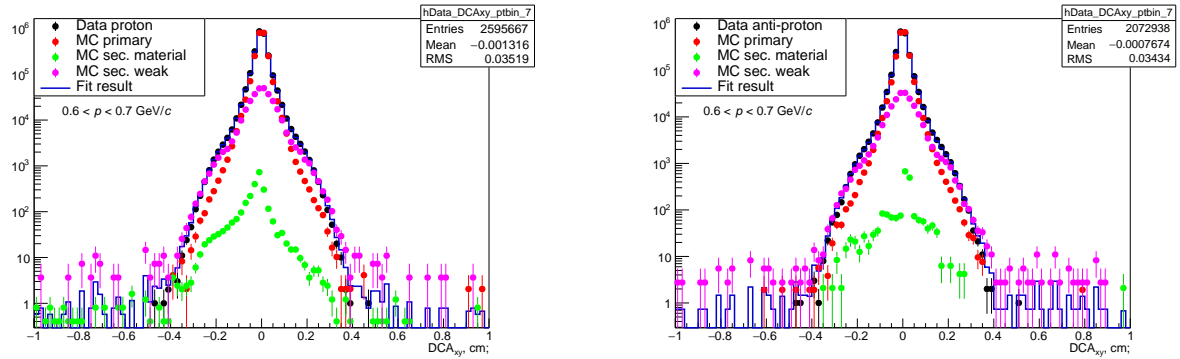


Fig. 23: DCA_{xy} distribution of proton (left) and anti-proton (right) candidates in momentum bin $0.6 < p < 0.7 \text{ GeV}/c$ along with MC templates for primaries, secondaries from material and secondaries from weak decays which are fitted to the data.

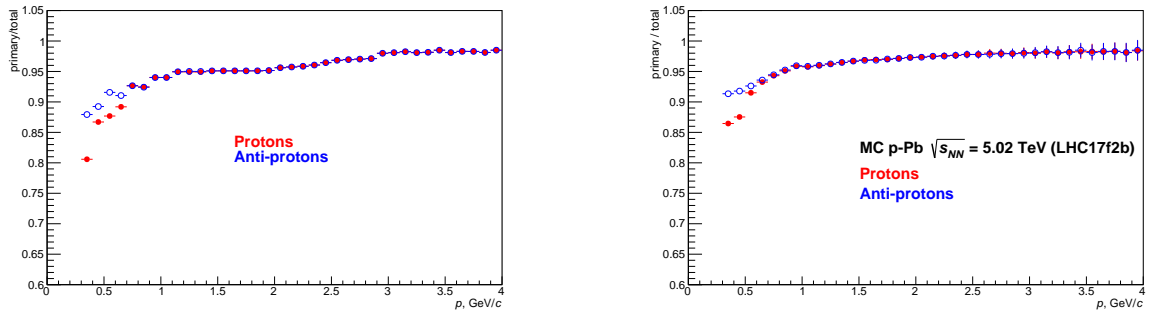


Fig. 24: Fraction of primary (anti-)protons as a function of momentum in experimental data (left) and in Monte Carlo simulations (right).

284 4.3 Anti-Particle To Particle Ratios

285 After the correction procedures described above, raw primary (anti-)particle spectra are used to build
 286 the ratios of anti-particles to particles. The results are shown in Fig. 27 for raw primary \bar{p}/p and \bar{d}/d
 287 ratios with statistical uncertainties only. The ratios show clear deviations from unity, indicating higher
 288 loss of primary anti-particles in detector material than of particles, especially in the momentum region
 289 where TOF PID is used for each track ($p > 0.7 \text{ GeV}/c$ for (anti-)protons and $p > 1.4 \text{ GeV}/c$ for (anti-
 290 deuterons). Stability of results is tested against several systematic cross-checks as described in the next
 291 Section.

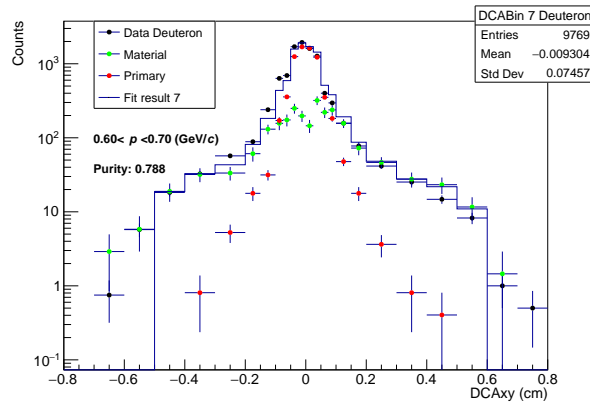


Fig. 25: DCA_{xy} distribution of deuteron candidates in momentum bin $0.6 < p < 0.7 \text{ GeV}/c$ along with template for primary deuterons (experimental anti-deuteron distribution) and MC templates for secondaries from material which are fitted to the data.

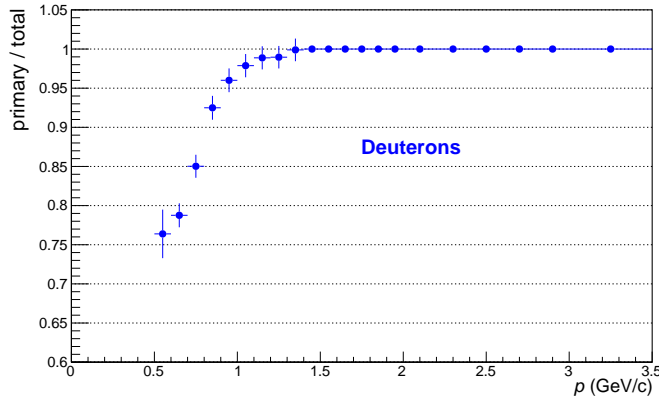


Fig. 26: Fraction of primary deuterons as a function of momentum in experimental data.

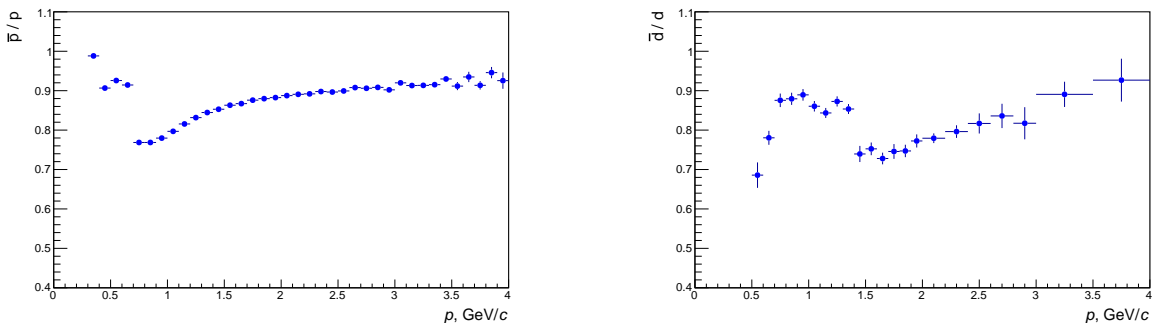


Fig. 27: Raw primary anti-proton to proton (left) and anti-deuteron to deuteron (right) ratios as a function of momentum. Only statistical uncertainties are shown.

292 **5 Systematic Checks and Uncertainties**

293 This Section describes cross-checks and evaluation of systematic uncertainties done in the analysis. Different aspects of the analysis are considered as possible sources for systematic uncertainty: tracking,
294 particle identification, fit procedure used to extract raw signal and corrections due to secondary particles.
295

296 **5.1 Tracking**

297 In order to test the stability of results against tracking requirements, analysis has been redone using 20
298 different track cut settings, which have been composed randomly from 3 possible variations for each cut
299 variable ("loose", "default" and "tight", see Table 5). To this purpose, `AliESDtrackCuts` class of Ali-
300 Root has been used to vary tracking requirements, and the method `AliESDtrackCuts::IsSelected()`
301 has been applied to AOD tracks. "Default" track cut values listed in Table 5 correspond to AOD Filter
302 Bit 256.

Table 5: Track cut variations used for systematic studies

Variable	Loose	Default	Tight
TPC crossed rows	50	70	110
Ratio crossed rows over find.	0.5	0.8	0.9
Max. χ^2 TPC	6.0	4.0	3.0
Max. fraction of shared TPC clusters	1.0	0.4	0.1
Max. χ^2 TPC constrained to global	49.0	36.0	25.0
SPD cluster requirements	-//-	Hit in any of 2 layers	Hit in first SPD layer
Min. number of ITS clusters	1	2	3
Max. χ^2 ITS	49.0	36.0	25.0

303 The impact of DCA_{xy} and DCA_z cut variations has been investigated separately and is included into
304 systematic uncertainty due to contamination from secondaries (see Section 5.3). However, different track
305 selection requirements listed in Table 5 imply different fraction of primary particles anyway (e.g. due
306 to looser/tighter selection on the number of ITS clusters or ITS χ^2 value), so the procedure described
307 in Section 4.2 has been redone for each track variation as well. The resulting anti-particle to particle
308 ratios are shown in Fig. 28 for all 20 cut variations. This procedure has been repeated in Monte Carlo
309 data analysis with the same 20 track selection requirements, and the RMS of relative differences in final
310 ratios between data and MC results has been taken into account as systematic uncertainty due to track
311 cuts variation. In order to suppress the statistical fluctuations in (anti-)deuteron analysis, this uncertainty
312 has been evaluated in large momentum bins of $0.5 \text{ GeV}/c$ (Fig. 35).

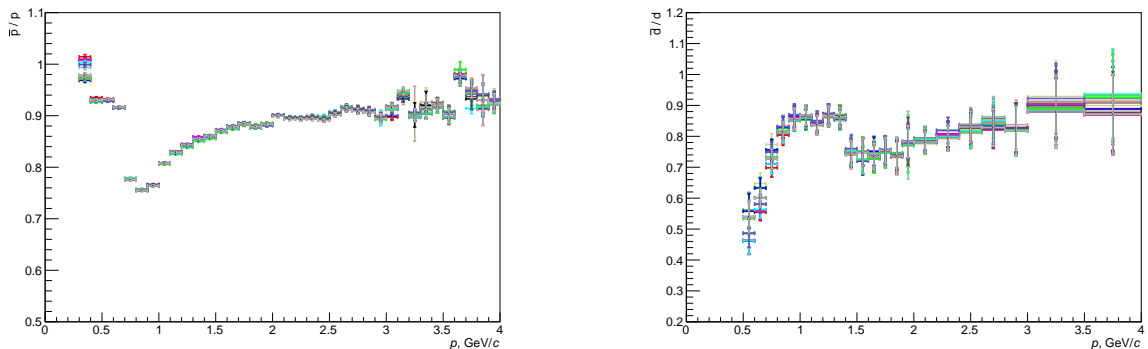


Fig. 28: Anti-proton to proton (left) and anti-deuteron to deuteron (right) ratios in experimental data corresponding to 20 different track selection criteria.

The ITS-TPC matching efficiency has been estimated for (anti-)protons and (anti-)deuterons as the ratio of number of tracks with ITS-TPC tracking requirements over the number of tracks with only TPC tracking requirements. Both TPC and ITS tracking requirements correspond to AOD Filter Bit 256, and the same tight DCA cuts have been used as in main analysis (Table 2). In order to minimise the impact of PID mis-identification at high momentum, PID requirements included also TOF selection as it is listed in Table 4. The results in experimental data are shown in Fig. 29 for (anti-)protons and (anti-)deuterons as a function of track momentum. Since the ITS-TPC matching is evaluated using strict sub-samples of experimental data (tracks passing ITS-TPC requirements vs. tracks passing TPC requirements only), the errors have been calculated using bayesian method. The same analysis has been done in Monte Carlo data, and the results are shown in Fig. 30. Since the relative difference in ITS-TPC matching between particles and anti-particles is not perfectly reproduced in Monte Carlo, the relative deviation between experimental and Monte Carlo results has been taken as systematic uncertainty.

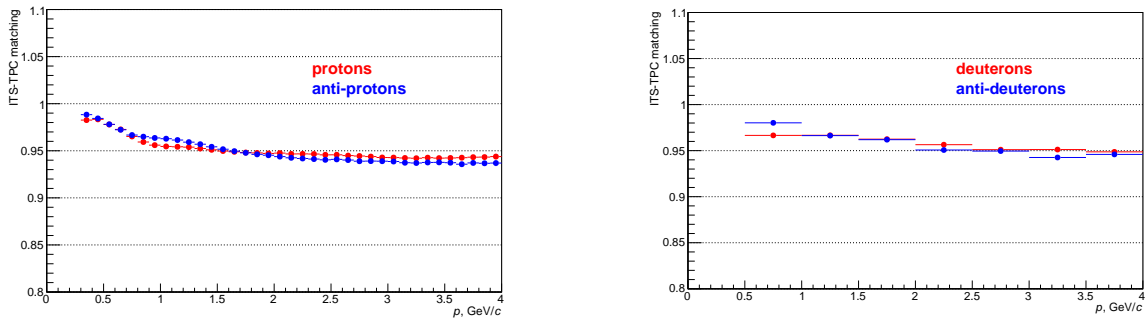


Fig. 29: ITS-TPC matching efficiency for (anti-)proton (left) and (anti-)deuteron (right) tracks as a function of track momentum in experimental data.

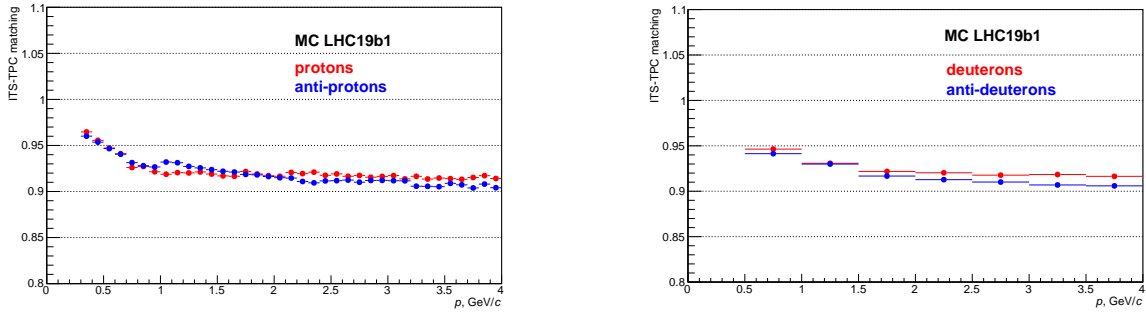


Fig. 30: ITS-TPC matching efficiency for (anti-)proton (left) and (anti-)deuteron (right) tracks as a function of track momentum in Monte Carlo data.

During both data taking periods LHC16q and LHC16t the magnetic field polarity in the ALICE central barrel has been set to $++$. Since azimuthal coverage of sub-detectors used in the analysis is not perfect, this can lead to different reconstruction efficiencies for positive and negative tracks and therefore to a bias in resulting anti-particle to particle ratios. As a cross-check, anti-proton to proton ratio has been re-analysed using data from two data taking periods from proton-proton collisions at $\sqrt{s} = 13$ TeV, LHC17i (field polarity $--$) and LHC17j (field polarity $++$). A “flip” between two periods can be seen in Fig. 31, which shows mean number of ITS clusters for proton and anti-proton candidates. The resulting anti-proton to proton ratios for two periods are shown in Fig. 32. The ratio between the results is fitted with a constant function, yielding in a $+0.68\%$ change. The effect of magnetic field polarity has been also investigated in Monte Carlo data using the corresponding samples anchored to LHC17i and LHC17j periods (LHC17k4 and LHC17h11, correspondingly). The resulting difference between two periods in this case amounts to $+1.27\%$ (Fig. 33). This leads to a global systematic uncertainty of 0.6% (relative

difference between experimental data and MC results), which is assigned to all data points for both anti-proton to proton and anti-deuteron to deuteron ratios.

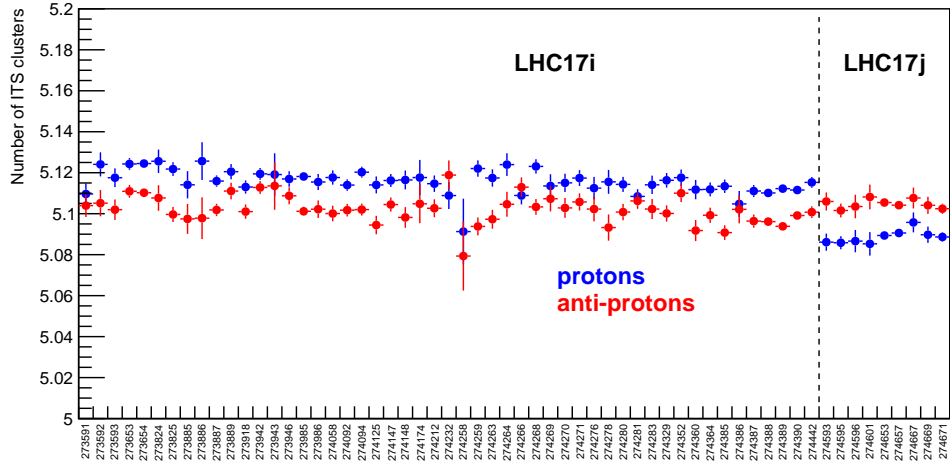


Fig. 31: Mean number of ITS clusters as a function of run number in LHC17i and LHC17j periods.

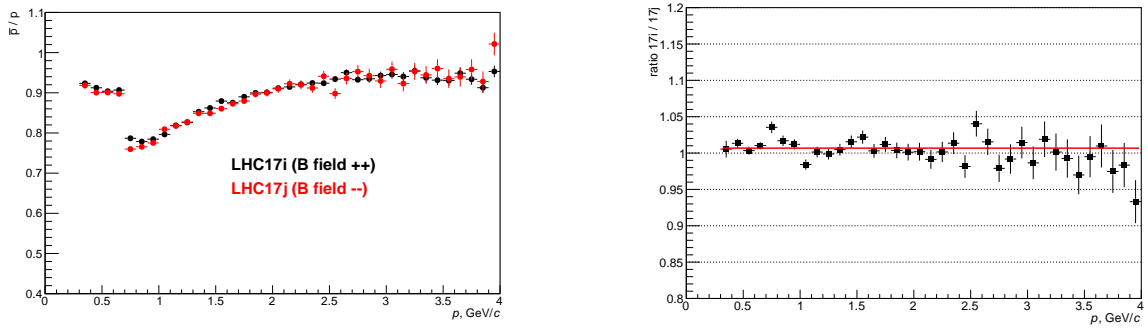


Fig. 32: Anti-proton to proton ratios in LHC17i and LHC17j periods (pp collisions at $\sqrt{s} = 13$ TeV, left) and the ratio of the results for two periods (right).

Another possible source of uncertainty due to detector geometry comes from the matching between TPC and TOF detectors. Similar to ITS-TPC matching, slightly different reconstruction efficiencies for positive and negative tracks can come from non-perfect azimuthal coverage of sub-detectors. In order to minimise the effect of (anti-)particle absorption in the TRD material, this check is performed with charged pions. In experimental data analysis, pions are selected with $\pm 3\sigma$ cut on TPC PID, whereas in Monte Carlo data pions are selected with usage of true Monte Carlo information. A fraction of tracks with matched TOF hit as a function of momentum is shown in Fig. 34, and small relative difference between Monte Carlo and experimental data analyses is taken into account for total systematic uncertainty due to tracking. This uncertainty is assigned only in the momentum range where TOF PID is used in the analysis ($p > 0.7$ GeV/c for (anti-)protons and $p > 1.4$ GeV/c for (anti-)deuterons).

Summary of all sources of systematic uncertainties due to tracking is shown in Fig. 35 for anti-proton to proton and anti-deuteron to deuteron ratios. The values of each uncertainty source in three typical momentum bins (lowest, first bin with TOF analysis, highest) are summarised also in Tables 6 and 7. For total uncertainty due to tracking individual sources have been added in quadrature.

5.2 PID selection

TPC PID selection is applied in the analysis to all tracks in whole investigated momentum region according to Table 3. For systematic studies, the maximum absolute value of $TPCn\sigma_{p,d}$ is varied between 2.0

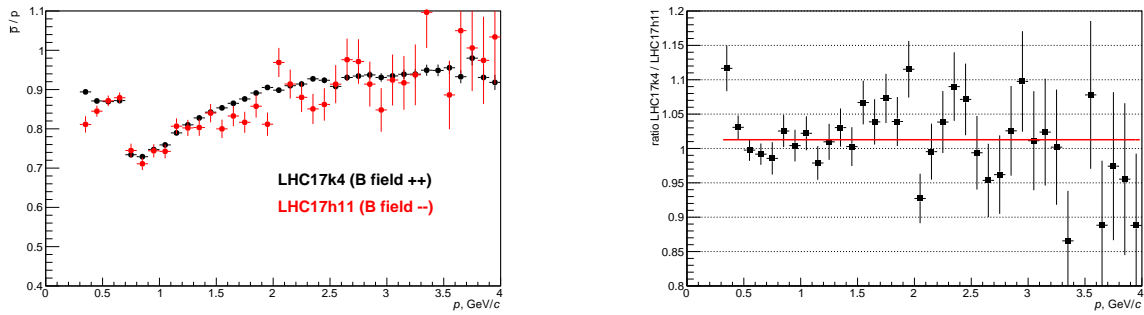


Fig. 33: Anti-proton to proton ratios in LHC17k4 and LHC17h11 Monte Carlo data (left) and the ratio of the results for two periods (right).

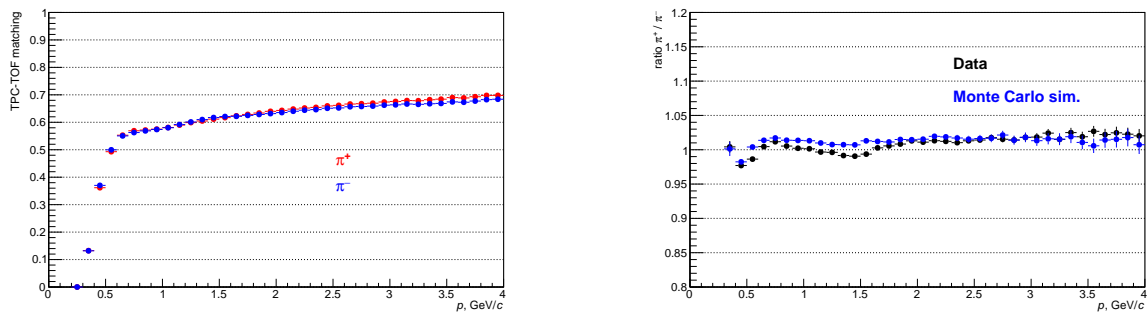


Fig. 34: Left: TPC-TOF matching efficiency for charged pions in experimental data as a function of track momentum. Right: ratio between the results in experimental data and Monte Carlo simulations.

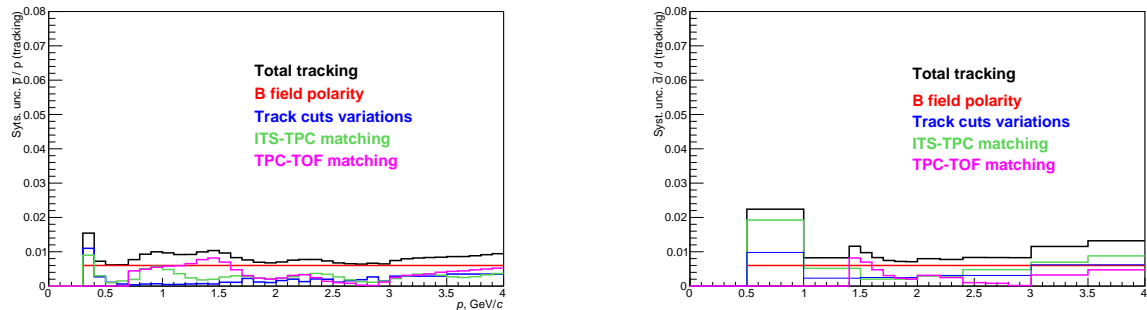


Fig. 35: Systematic uncertainty due to tracking for \bar{p}/p (left) and \bar{d}/d (right) as a function of momentum.

356 (“tight”), 3.0 (“default”) and 4.0 (“loose”), both for (anti-)protons and for (anti-)deuterons. The resulting
 357 variations of raw proton and deuteron spectra are shown in Fig. 36. Deviations of raw (anti-)particle
 358 ratios obtained in this way from the default one have been also investigated in Monte Carlo simulations,
 359 and the relative maximum difference between experimental experimental results and Monte Carlo
 360 simulations has been included into final systematic uncertainty.

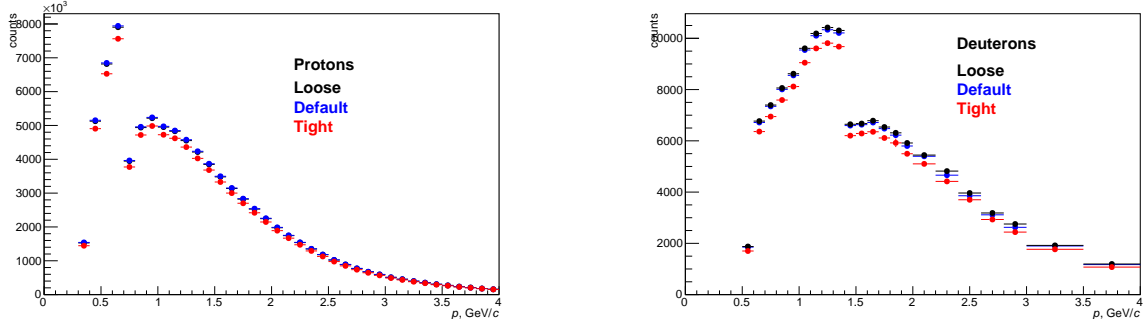
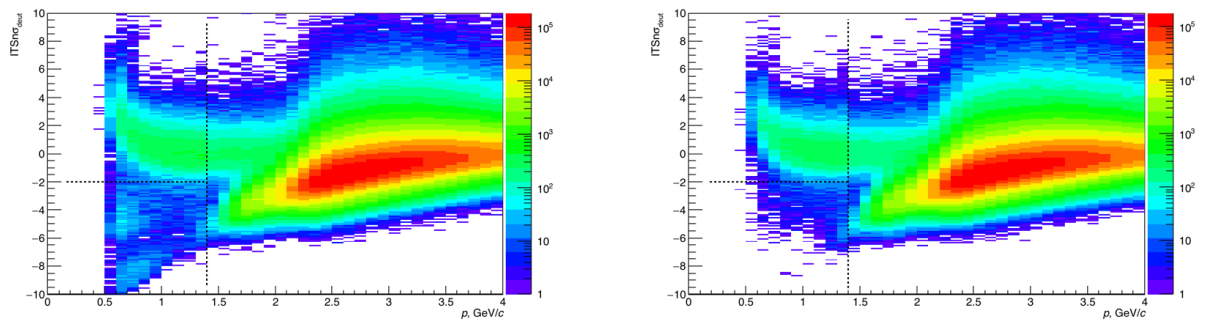
361 In addition to TPC PID selection, for (anti-)deuteron analysis the ITS PID requirements are applied
 362 up to momentum $p = 1.4\text{ GeV}/c$ (Table 3). The purpose of this cut is to reject some secondary bands
 363 visible in $ITSn\sigma_d$ distribution at low momentum for deuterons, but not for anti-deuterons (Fig. 38). To
 364 investigate the characteristics of these tracks in more details, deuteron candidates with momentum below
 365 $p = 1.4\text{ GeV}/c$ have been divided into two subsamples: with $ITSn\sigma_d > -2$ (“good” tracks) and with
 366 $ITSn\sigma_d < -2$ (“bad” tracks). Although DCA_{xy} distributions for two sub-samples have been found to be
 367 similar and to peak at zero, ITS χ^2 value as well as fraction of tracks with shared ITS cluster have been
 368 found to be significantly worse for second “bad” subsample (Fig. 38).

Table 6: Values of tracking systematic uncertainty for (anti-)protons

Source	$p = 0.3 \text{ GeV}/c$	$p = 0.7 \text{ GeV}/c$	$p = 4.0 \text{ GeV}/c$
B field polarity	0.6%	0.6%	0.6%
Track cuts variations	1.1%	0.0%	0.4%
ITS-TPC matching	0.9%	0.2%	0.4%
TPC-TOF matching	0.0%	0.4%	0.5%
Total	1.5%	0.8%	0.9%

Table 7: Values of tracking systematic uncertainty for (anti-)deuterons

Source	$p = 0.5 \text{ GeV}/c$	$p = 1.4 \text{ GeV}/c$	$p = 4.0 \text{ GeV}/c$
B field polarity	0.6%	0.6%	0.6%
Track cuts variations	1.0%	0.2%	0.6%
ITS-TPC matching	1.9%	0.2%	0.9%
TPC-TOF matching	0.0%	0.8%	0.5%
Total	2.2%	1.1%	1.3%

**Fig. 36:** Raw spectra for protons (left) and deuterons (right) corresponding to 3 different TPC PID selection criteria in experimental data analysis.**Fig. 37:** ITSn σ_d distribution as a function of track momentum for deuteron (left) and anti-deuteron (right) candidates after TPC and TOF PID selection listed in Table 3. Vertical dashed line indicates momentum up to which ITS PID selection is applied ($\text{ITSn}\sigma_d > -2$, horizontal line).

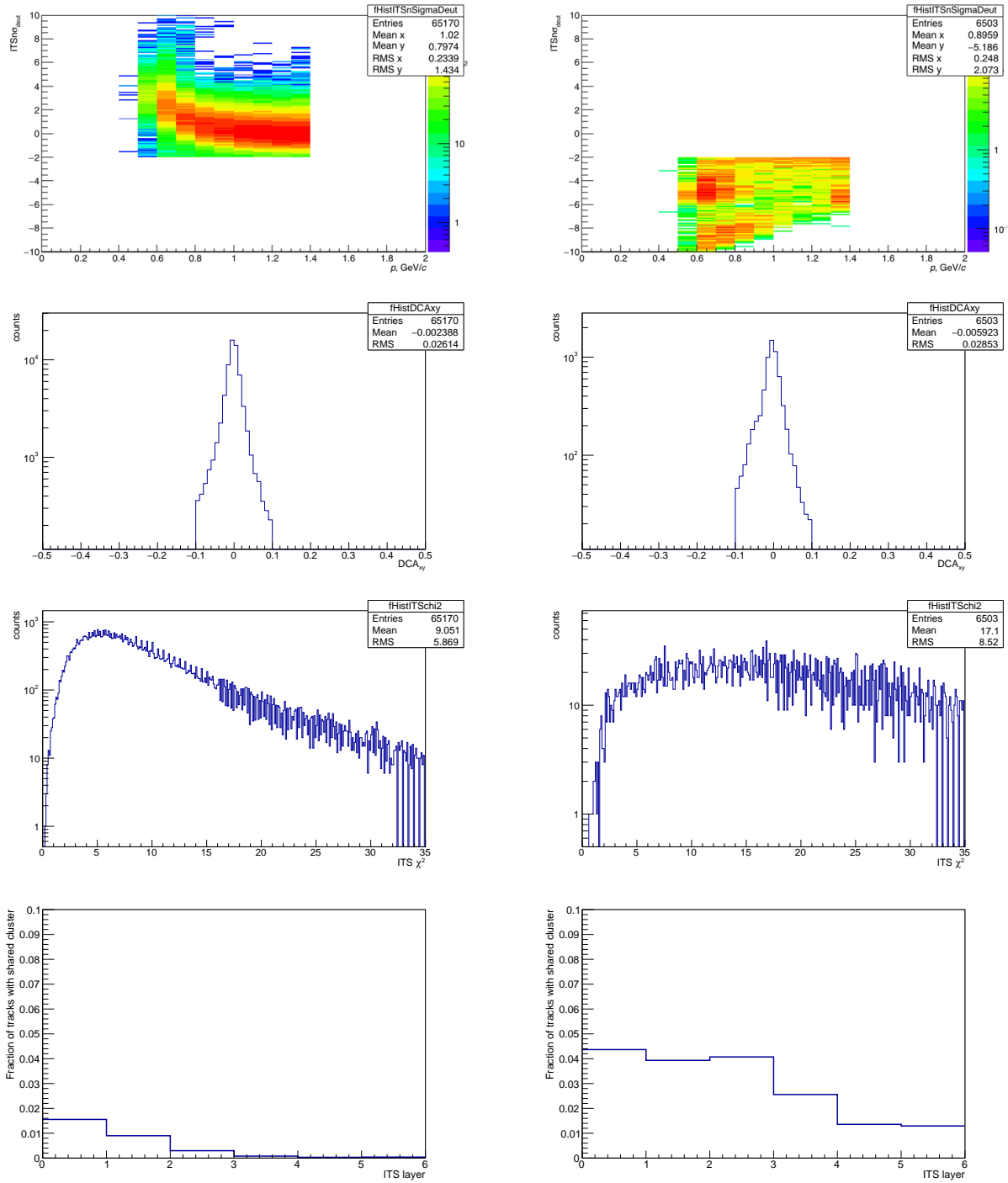


Fig. 38: Comparison of deuteron candidates at low momentum with $\text{ITS}n\sigma_{\text{d}} > -2$ (“good” tracks, left) and with $\text{ITS}n\sigma_{\text{d}} < -2$ (“bad” tracks, right). Top row: $\text{ITS}n\sigma_{\text{d}}$, second row: DCA_{xy} distribution, third row: $\text{ITS}\chi^2$ value, bottom row: fraction of tracks with at least one shared ITS cluster.

As a result of these checks, a requirement of $\text{ITSn}\sigma_d > -2.0$ is applied both to deuteron and anti-deuteron candidates up to momentum $p = 1.4 \text{ GeV}/c$. For systematic studies this cut value is varied between -3.0 (“loose”), -2.0 (“default”) and -1.0 (“tight”), and the resulting deviations of anti-deuteron to deuteron ratios from the default one are included into systematic uncertainty (Fig. 39).

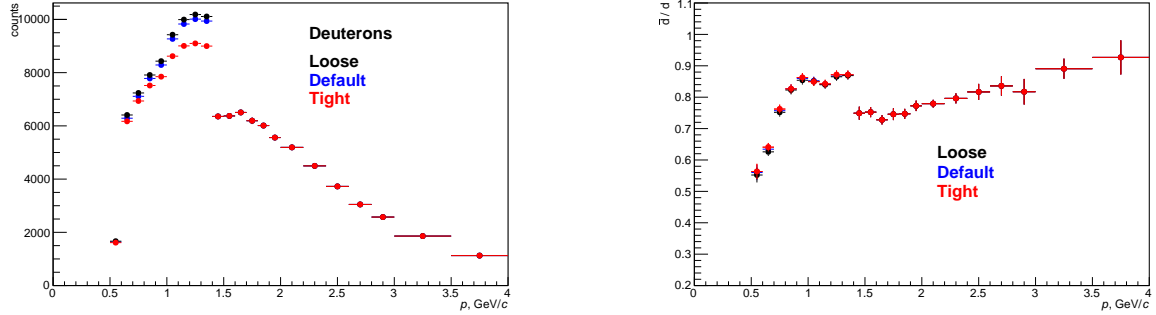


Fig. 39: Raw deuteron spectra (left) and anti-deuteron to deuteron ratios (right) corresponding to 3 different ITS PID selection criteria as explained in text.

At higher momentum particle identification is performed with help of TOF detector, and raw signal yield is extracted by using fits to TOFm^2 distributions as described in Section 4.1. For systematic studies the fit range and the bin size of input TOFm^2 histograms have been varied according to Table 8. As an example of this procedure, resulting raw deuteron spectra and anti-deuteron to deuteron ratios are shown in Fig. 40. The systematic uncertainty due to TOF PID is shown in Fig. 41 for anti-proton to proton and anti-deuteron to deuteron ratios, for which individual contributions from TOFm^2 fit ranges and from bin size variations are added in quadrature. For (anti-)proton analysis, also the variation of TOF PID selection used in the momentum range of $0.7 < p < 2.5 \text{ GeV}/c$ has been investigated in experimental data and in Monte Carlo simulations (varying the selection criteria between $\pm 1.5\sigma$, $\pm 2.0\sigma$ and $\pm 3.0\sigma$), and the maximum relative difference between the results has been taken as systematic uncertainty.

Table 8: Variation of TOFm^2 fit parameters

Parameter	Wide	Default	Tight
Fit range (protons), $(\text{GeV}/c^2)^2$	(0.1, 2.2)	(0.2, 2.0)	(0.3, 1.8)
Fit range (deuterons), $(\text{GeV}/c^2)^2$	(1.7, 5.3)	(2.0, 5.0)	(2.3, 4.7)
Bin size, $(\text{GeV}/c^2)^2$	0.04	0.02	0.01

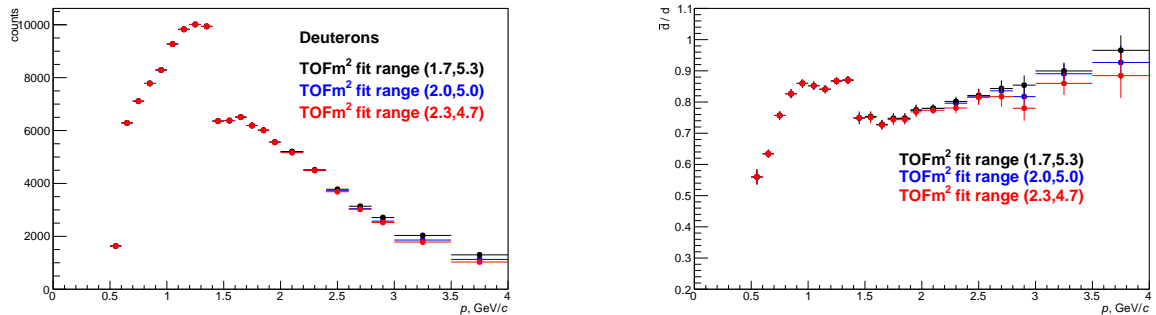


Fig. 40: Raw deuteron spectra (left) and anti-deuteron to deuteron ratios (right) corresponding to 3 different TOFm^2 fit ranges as explained in text.

Total systematic uncertainty due to particle identification used in analysis is shown in Fig. 42 together with separate contributions from ITS (for \bar{d}/d ratio only), TPC and TOF analyses. For total uncertainty due to particle identification, individual sources have been added in quadrature.

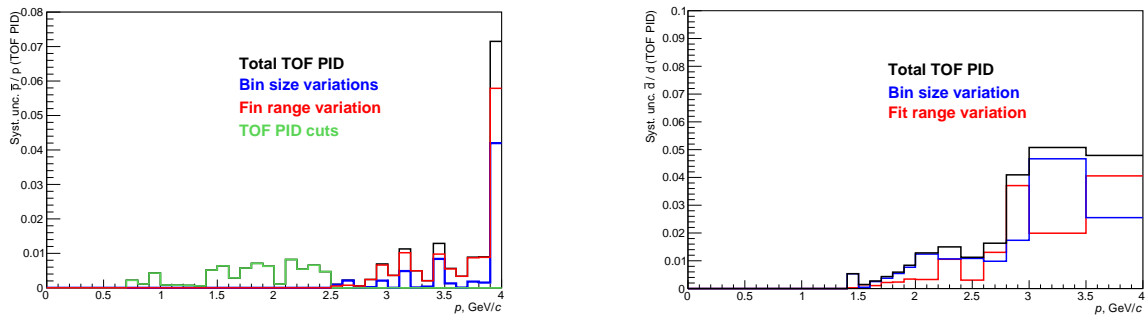


Fig. 41: Systematic uncertainty due to TOF PID for \bar{p} / p (left) and \bar{d} / d (right) as a function of momentum.

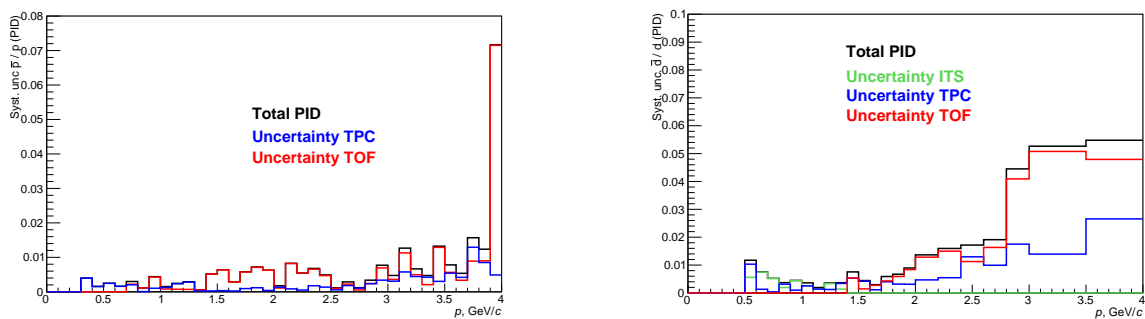


Fig. 42: Total systematic uncertainty due to particle identification for \bar{p} / p (left) and \bar{d} / d (right) as a function of momentum.

386 5.3 Secondary Particles

387 Fraction of secondary particles is estimated in the analysis with help of fits to DCA_{xy} distributions as
 388 discussed in Section 4.2. For systematic studies the fit range has been varied between $(-1.5, 1.5)$,
 389 $(-1.0, 1.0)$ and $(-0.5, 0.5)$ cm and the histogram bin size between $0.01 \text{ GeV}/c$ and $0.02 \text{ GeV}/c$. The
 390 signal template function has been flipped between particles and anti-particles (for deuterons Monte Carlo
 391 template of primary deuterons has been used instead of experimental anti-deuteron distribution), and the
 392 fit has been repeated again. DCA cuts used in the analysis have been varied according to Table 9, and
 393 the maximum relative difference between the final results in experimental data and in Monte Carlo anal-
 394 ysis has been assigned as uncertainty. The resulting systematic uncertainties of final ratios are shown in
 395 Fig. 43.

Table 9: DCA cut variations used for systematic studies

Variable	Loose	Default	Tight
DCA_{xy}	0.5 cm	0.1 cm	0.05 cm
DCA_z	1.0 cm	0.2 cm	0.1 cm

396 5.4 Total systematic uncertainty

397 Finally, all sources of systematic uncertainties discussed above (tracking, particle identification and
 398 DCA_{xy} fit procedure) are added in quadrature, and the resulting total systematic uncertainty is shown
 399 in Fig. 44. The values of each uncertainty source in three typical momentum bins (lowest, first bin with
 400 TOF analysis, highest) are summarised also in Tables 10 and 11.

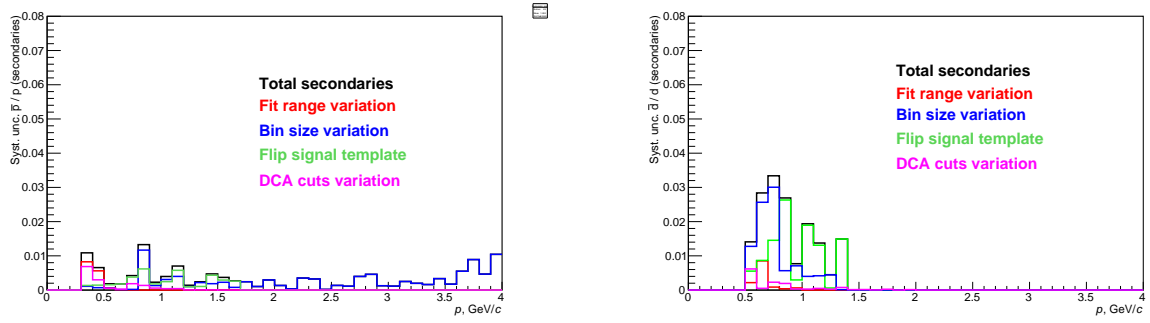


Fig. 43: Total systematic uncertainty due to secondary particles for \bar{p} / p (left) and \bar{d} / d (right) as a function of momentum.

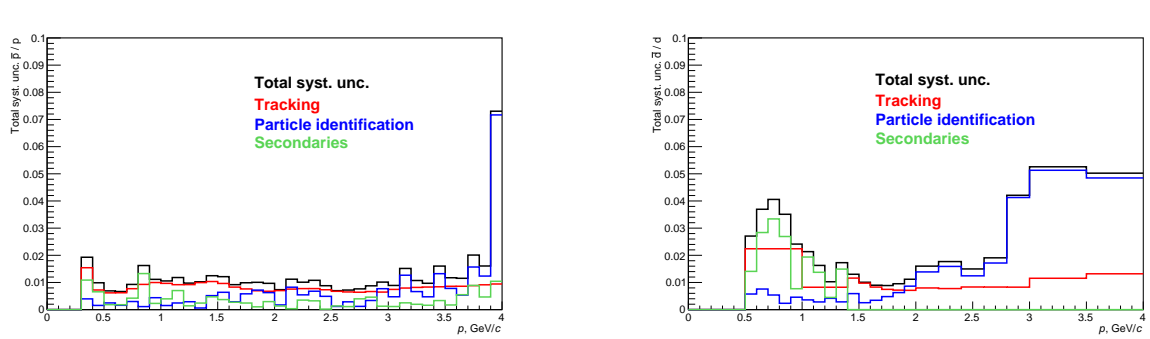


Fig. 44: Total systematic uncertainty for \bar{p} / p (left) and \bar{d} / d (right) as a function of momentum.

Table 10: Total systematic uncertainty for (anti-)proton analysis

Source	$p = 0.3 \text{ GeV}/c$	$p = 0.7 \text{ GeV}/c$	$p = 4.0 \text{ GeV}/c$
Tracking	1.5%	0.8%	0.9%
Particle identification	0.4%	0.3%	1.2%
Secondaries	1.1%	0.4%	0.5%
Total	1.9%	0.9%	1.6%

Table 11: Total systematic uncertainty for (anti-)deuteron analysis

Source	$p = 0.5 \text{ GeV}/c$	$p = 1.4 \text{ GeV}/c$	$p = 4.0 \text{ GeV}/c$
Tracking	2.2%	1.0%	1.3%
Particle identification	0.6%	0.6%	5.1%
Secondaries	1.4%	1.5%	0.0%
Total	2.7%	1.3%	5.2%

5.5 Global Uncertainty From Primordial Ratio

At LHC energies, matter and anti-matter are produced in high-energy collisions in essentially equal abundance at mid-rapidity. In [3] corrected anti-proton to proton ratio has been measured in proton–proton collision at various collision energies, and the resulting ratio (integrated over mid-rapidity) amounts to (Fig. 45):

- $\sqrt{s} = 0.9 \text{ TeV}$: $R = 0.957 \pm 0.006 \text{ (stat.)} \pm 0.014 \text{ (syst.)}$
- $\sqrt{s} = 2.76 \text{ TeV}$: $R = 0.977 \pm 0.002 \text{ (stat.)} \pm 0.014 \text{ (syst.)}$
- $\sqrt{s} = 7 \text{ TeV}$: $R = 0.991 \pm 0.005 \text{ (stat.)} \pm 0.014 \text{ (syst.)}$

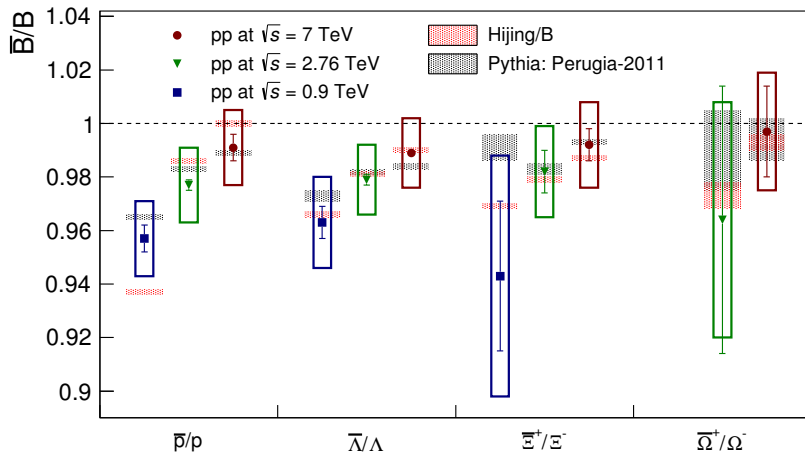


Fig. 45: The mid-rapidity (anti-)baryon yields ratio integrated over $|y| < 0.5$ in proton–proton collisions at different collision energies [3].

409 Extrapolated linearly to $\sqrt{s} = 5$ TeV collision energy, this ratio amounts to 0.984 ± 0.015 for \bar{p}/p ratio
 410 and to 0.968 ± 0.030 for \bar{p}/p ratio (assuming that $(\bar{d}/d) \sim (\bar{p}/p)^2$). Therefore, a global uncertainty of
 411 1.5% (3.0%) has been taken into account for raw primary ratios of (anti-)protons (anti-)deuterons.

412 6 Ratio of Raw Primary Spectra

413 Fig. 46 shows raw primary \bar{p}/p and \bar{d}/d ratios with statistical and systematic uncertainties. Both ratios
 414 have been found to be significantly lower than unity, which indicates higher loss of primary anti-particles
 415 compared to particles. This effect is especially visible as a step at $p = 0.7\text{ GeV}/c$ for \bar{p}/p and at $p =$
 416 $1.4\text{ GeV}/c$ for \bar{d}/d , starting from which TOF PID information is used in the analysis — this means that
 417 each (anti-)particle has to penetrate at least the TRD detector ($X_0 \sim 24.7\%$) placed between TPC and
 418 TOF. At lower momentum, absorption of (anti-)particles is possible in beam pipe ($X_0 \sim 0.3\%$) as well
 419 as in ITS ($X_0 \sim 8.0\%$) and TPC ($X_0 \sim 4.0\%$) detectors.

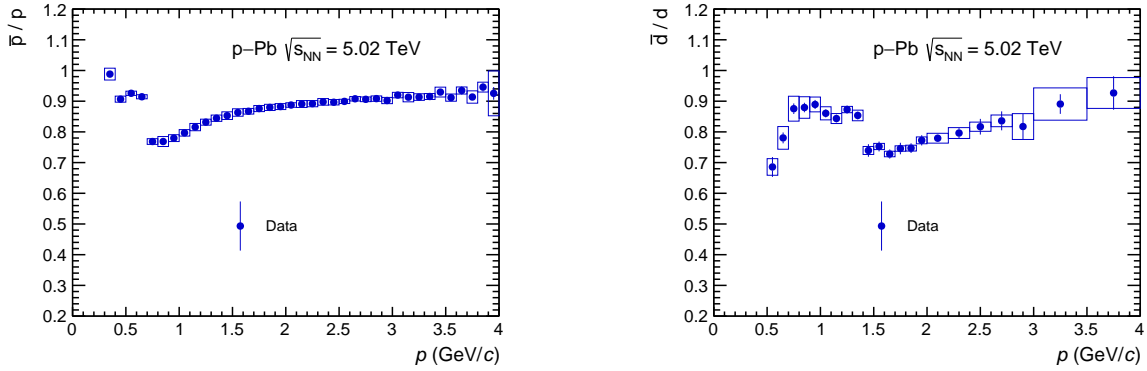


Fig. 46: Raw primary anti-proton to proton (left) and anti-deuteron to deuteron (right) ratios as a function of momentum. Statistical and systematic uncertainties are shown as vertical bars and boxes correspondingly.

420 The results have been compared to full-scale ALICE simulations using Geant3 and Geant4 toolkits for
 421 the propagation of (anti-)particles through the ALICE detector (Fig. 47). For this purpose, Nuclei Box
 422 Monte Carlo productions LHC19b1 (Geant4) and LHC19b1b (Geant3) have been used. Pure primary
 423 (anti-)protons and (anti-)deuterons have been selected on generated level by using true Monte Carlo
 424 information and the corresponding PDG code, and the same track and PID selection criteria as in ex-
 425 perimental data analysis (Tables 2 and 3) have been applied to reconstructed AOD tracks. Since in this
 426 Monte Carlo production anti-nuclei and nuclei have been injected in each event with a 1 : 1 ratio, the
 427 Monte Carlo results are scaled with a correction factor of 0.984 (0.968) for \bar{p}/p (\bar{d}/d) ratio as discussed
 428 in Section 5.5. The corresponding global uncertainty of 1.5% (3.0%) is not shown on the top plots,
 429 but is added in quadrature on the bottom plots together with statistical and systematic uncertainties of
 430 experimental data.

431 For \bar{p}/p ratio experimental data are in better agreement with Geant4 simulations in low momentum
 432 range and in agreement within uncertainties with both Geant versions above $p \sim 2\text{ GeV}/c$. For \bar{d}/d ratio
 433 Geant4-based simulations are clearly in better agreement with experimental data in most of momentum
 434 bins and are able to reproduce a step at $p = 1.4\text{ GeV}/c$ due to additional absorption in TRD detector.
 435 Since all other settings are the same between two used Monte Carlo productions, this indicates better
 436 description of (anti-)deuteron propagation in detector material implemented in Geant4, and first of all
 437 inelastic interaction cross-sections. For antinucleus–nucleus inelastic cross-sections, Geant3 exploits the
 438 parameterisations based on Moiseev’s empirical formula [4], whereas Geant4 relies on Glauber approach
 439 convoluted with Monte Carlo averaging method as described in [5]. An overview of Geant3 and Geant4
 440 parameterisations for (anti-)deuteron inelastic interaction cross-sections is shown in Fig. 48 together with
 441 the available experimental data, where a better agreement between Geant4 and experimental data can be
 442 seen.

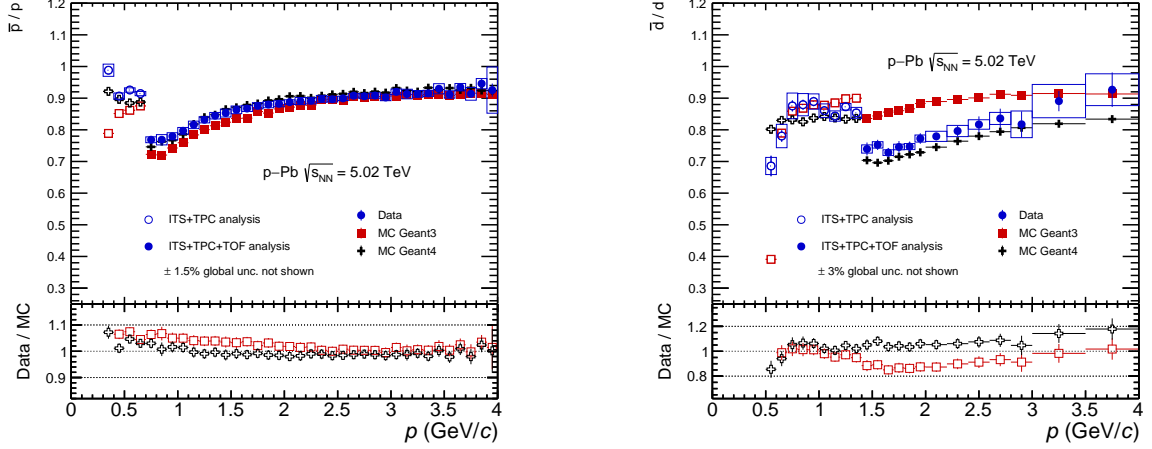


Fig. 47: Raw primary \bar{p}/p (left) and \bar{d}/d (right) ratios compared to full-scale ALICE simulations based on Geant3 and Geant4. Statistical and systematic uncertainties of experimental data are shown on the top plots as vertical bars and boxes correspondingly. The statistical uncertainties of Monte Carlo results are small and can be neglected. Bottom plots show the ratio between experimental data and Monte Carlo results, with errors corresponding to the quadratic sum of statistical, systematic and global uncertainties.

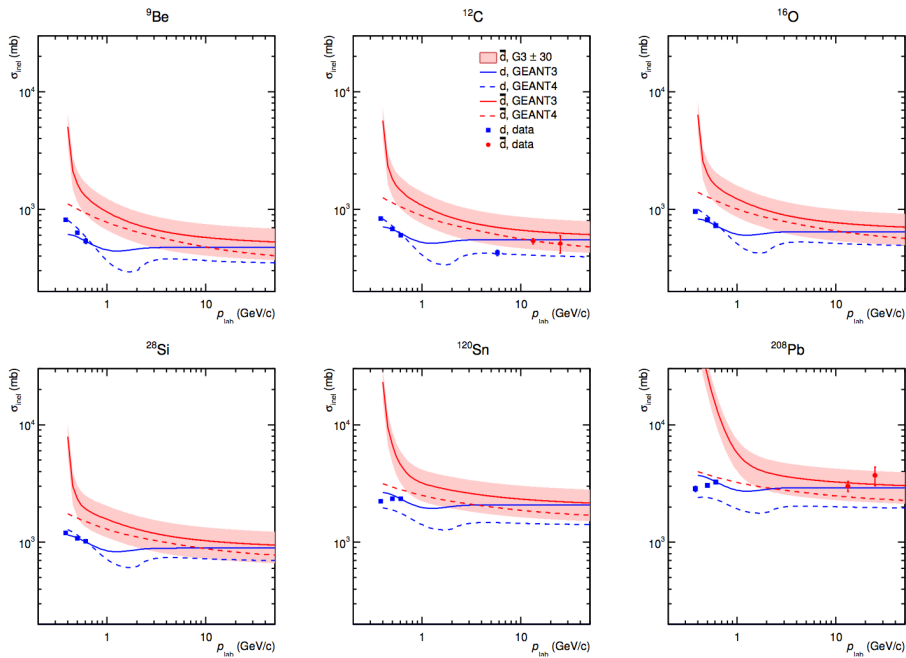


Fig. 48: Geant3 and Geant4 parametrisations of inelastic interaction cross-section of (anti-)deuterons on different materials. Figure is taken from [6], experimental data points are from [7–10]

443 7 Simple Geant4 Model

⁴⁴⁴ **8 Constraints on Anti-deuteron Inelastic Cross-section**

445 9 Plots for Approval

446 This Section summarises the plots aiming at approval as ALICE Preliminary results.

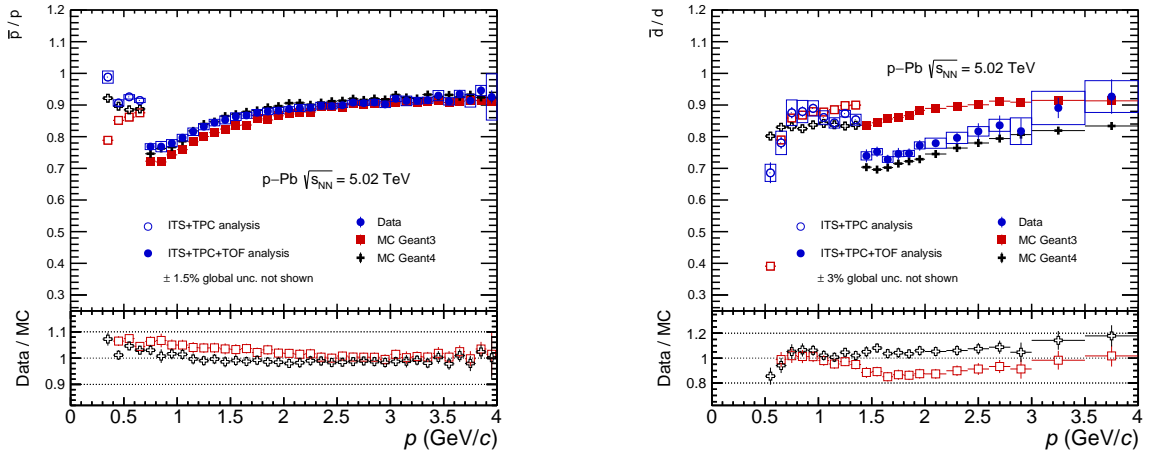


Fig. 49: ALICE Physics Preliminary candidate: raw primary \bar{p}/p (left) and \bar{d}/d (right) ratios compared to full-scale ALICE simulations based on Geant3 and Geant4. Statistical and systematic uncertainties of experimental data are shown on the top plots as vertical bars and boxes correspondingly. The statistical uncertainties of Monte Carlo results are small and can be neglected. Bottom plots show the ratio between experimental data and Monte Carlo results, with errors corresponding to the quadratic sum of statistical, systematic and global uncertainties.

References

- [1] S. Acharya *et al.* (ALICE), Nucl. Instrum. Meth. **A881**, 88 (2018), arXiv:1709.02743 [physics.ins-det].
- [2] M. Colocci, *(Anti-)deuteron production as a function of charged-particle multiplicity in pp collisions at 7 TeV*, ALICE Analysis Note ALICE-ANA-675 (PWG-LF, 2017).
- [3] E. Abbas *et al.* (ALICE), Eur. Phys. J. **C73**, 2496 (2013), arXiv:1305.1562 [nucl-ex].
- [4] A. A. Moiseev and J. F. Ormes, Astroparticle Physics **6**, 379 (1997).
- [5] V. Uzhinsky, J. Apostolakis, A. Galoyan, G. Folger, V. M. Grichine, V. N. Ivanchenko, and D. H. Wright, Phys. Lett. **B705**, 235 (2011).
- [6] E. S. Rodriguez, *Deuterons, antideuterons, antitritons and ${}^3\bar{\text{He}}$ nuclei in pp collisions at $\sqrt{s} = 900 \text{ GeV}, 2.76 \text{ TeV and } 7 \text{ TeV}$* , ALICE Analysis Note ALICE-ANA-161 (PWG-LF, 2014).
- [7] A. Auce, R. F. Carlson, A. J. Cox, A. Ingemarsson, R. Johansson, P. U. Renberg, O. Sundberg, and G. Tibell, Phys. Rev. **C53**, 2919 (1996).
- [8] J. Jaros *et al.*, Phys. Rev. **C18**, 2273 (1978).
- [9] F. G. Binon *et al.*, Phys. Lett. **31B**, 230 (1970).
- [10] S. P. Denisov, S. V. Donskov, Yu. P. Gorin, V. A. Kachanov, V. M. Kutjin, A. I. Petrukhin, Yu. D. Prokoshkin, E. A. Razuvaev, R. S. Shuvalov, and D. A. Stojanova, Nucl. Phys. **B31**, 253 (1971).

464 Appendices

465 A Quality Assurance

466 A.1 Run-by-run QA

467 The following figures show the results of run-by-run checks on track level for momentum-integrated
 468 deuteron and anti-deuteron candidates as discussed in Section 3.

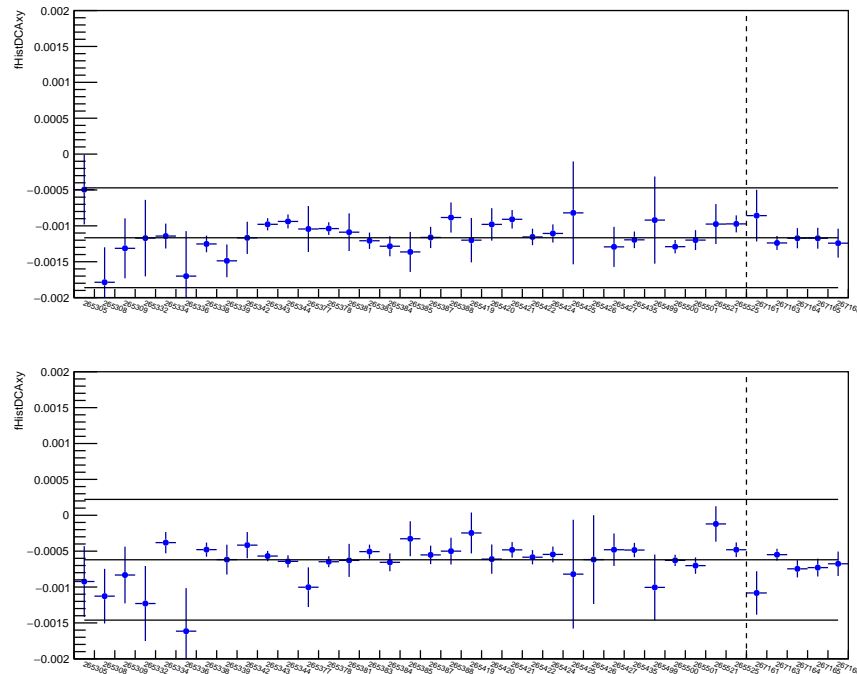


Fig. A.1: Mean DCA_{xy} for deuteron (top) and anti-deuteron (bottom) candidates as a function of run number.

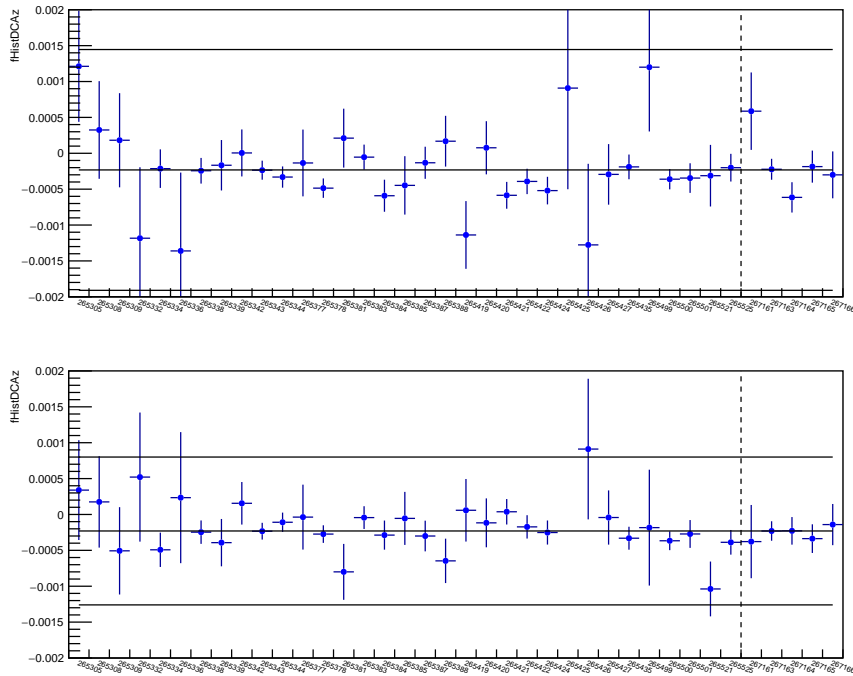


Fig. A.2: Mean DCA_z for deuteron (top) and anti-deuteron (bottom) candidates as a function of run number.

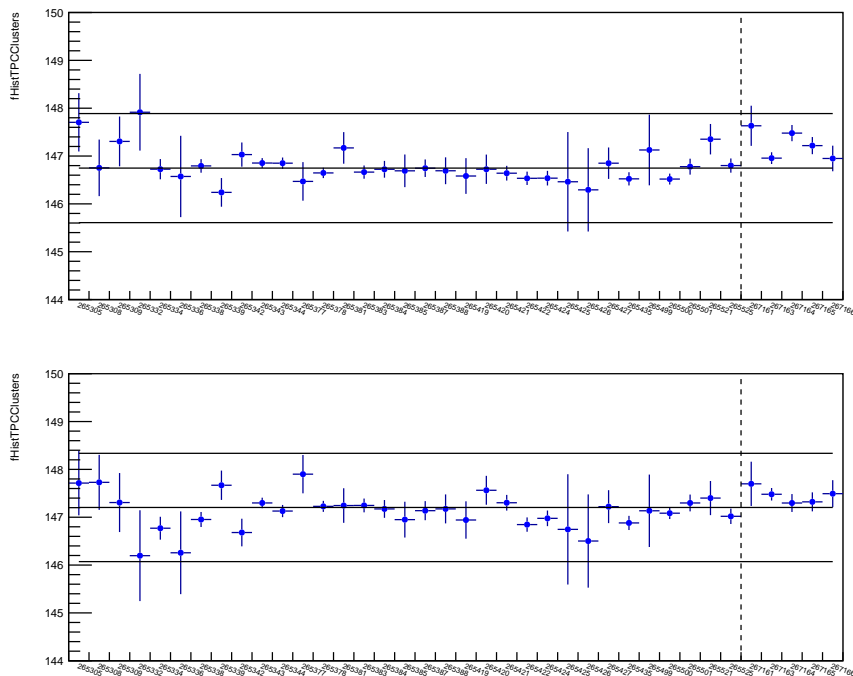


Fig. A.3: Mean number of TPC clusters for deuteron (top) and anti-deuteron (bottom) candidates as a function of run number.

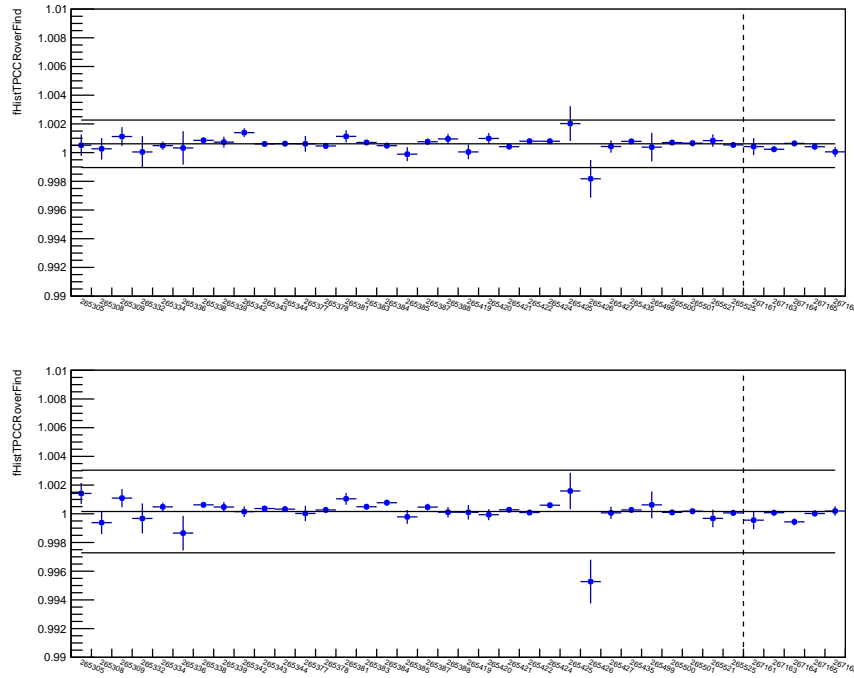


Fig. A.4: Mean ratio of TPC crossed rows over findable clusters for deuteron (top) and anti-deuteron (bottom) candidates as a function of run number.

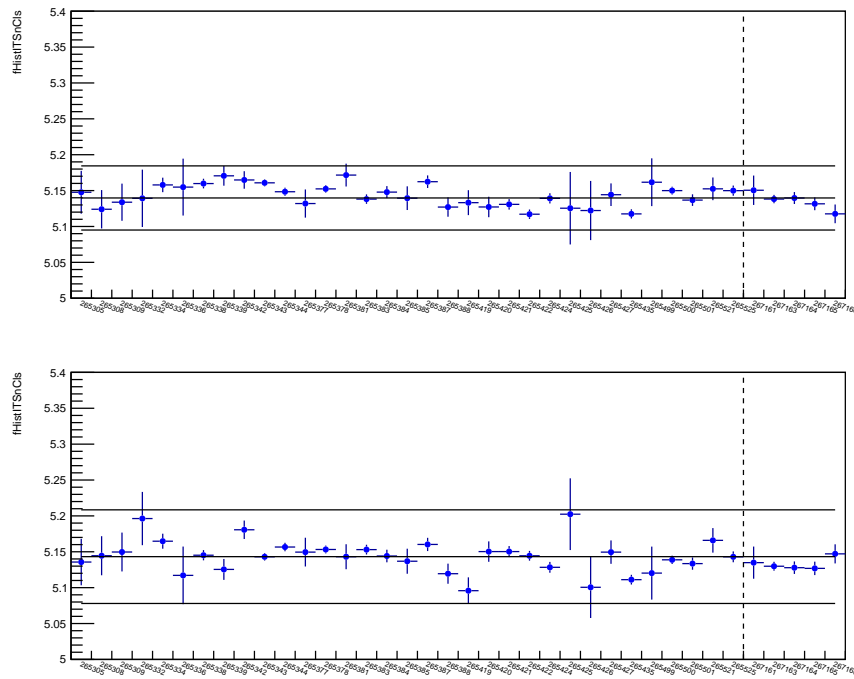


Fig. A.5: Mean number of ITS clusters for deuteron (top) and anti-deuteron (bottom) candidates as a function of run number.

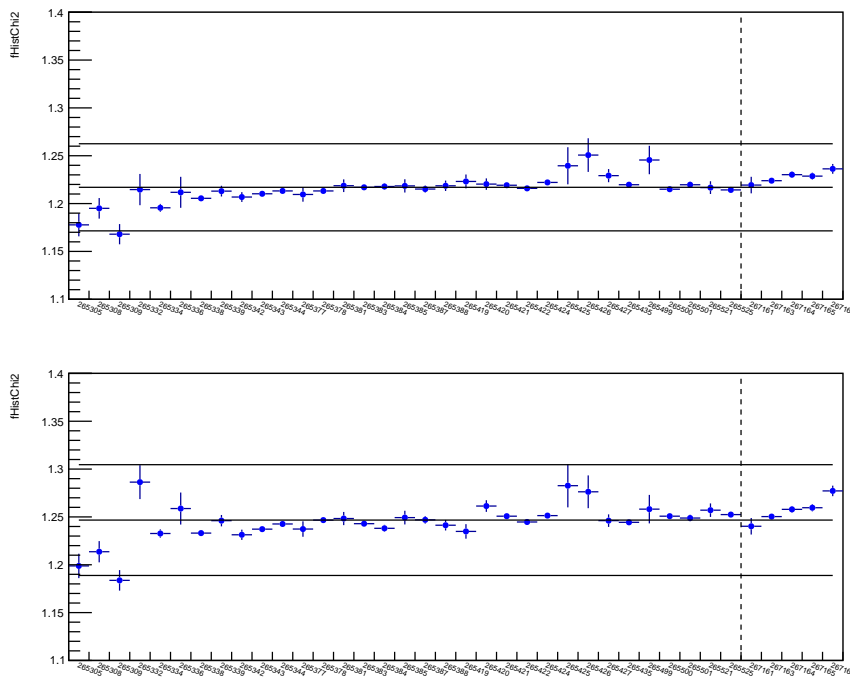


Fig. A.6: Mean TPC χ^2 value for deuteron (top) and anti-deuteron (bottom) candidates as a function of run number.

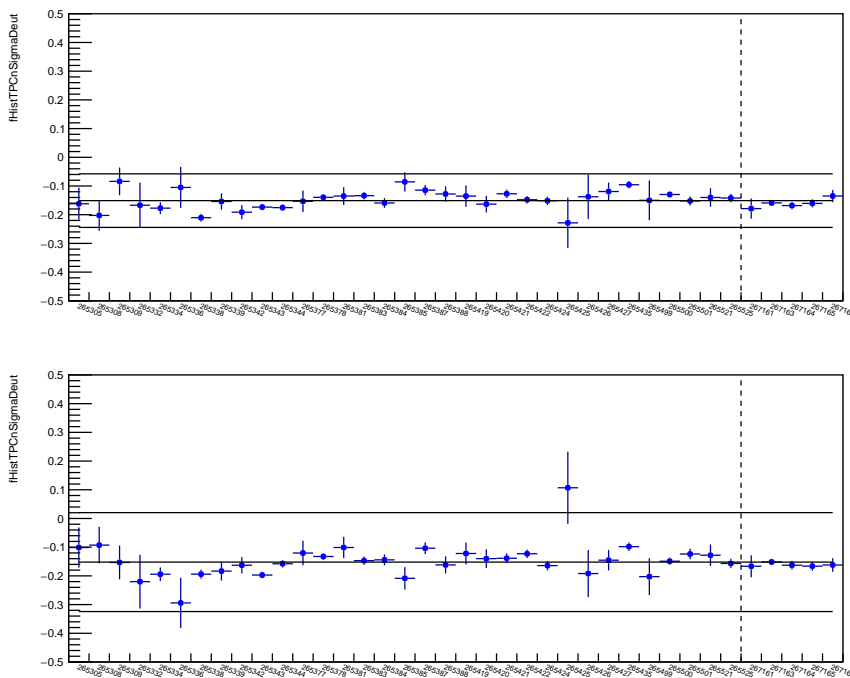


Fig. A.7: Mean TPC $n\sigma_d$ for deuteron (top) and anti-deuteron (bottom) candidates as a function of run number.

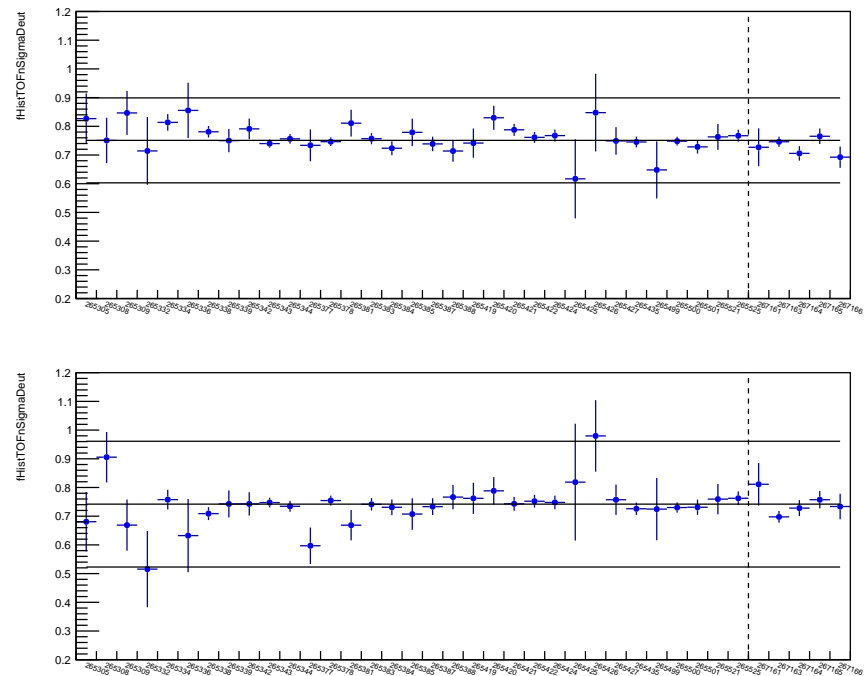


Fig. A.8: Mean $\text{TOFn}\sigma_d$ for deuteron (top) and anti-deuteron (bottom) candidates as a function of run number.

469 B TOF mass square fits

470 B.1 TOF m^2 fits for (anti-)protons

471 Following figures show fits to TOF m^2 distributions of (anti-)proton candidates in all analysed momentum
472 bins. The fit procedure is described in Section 4.1. For comparison, also TOF m^2 distributions from
473 Monte Carlo simulations are shown in all momentum bins below $p = 2.5 \text{ GeV}/c$.

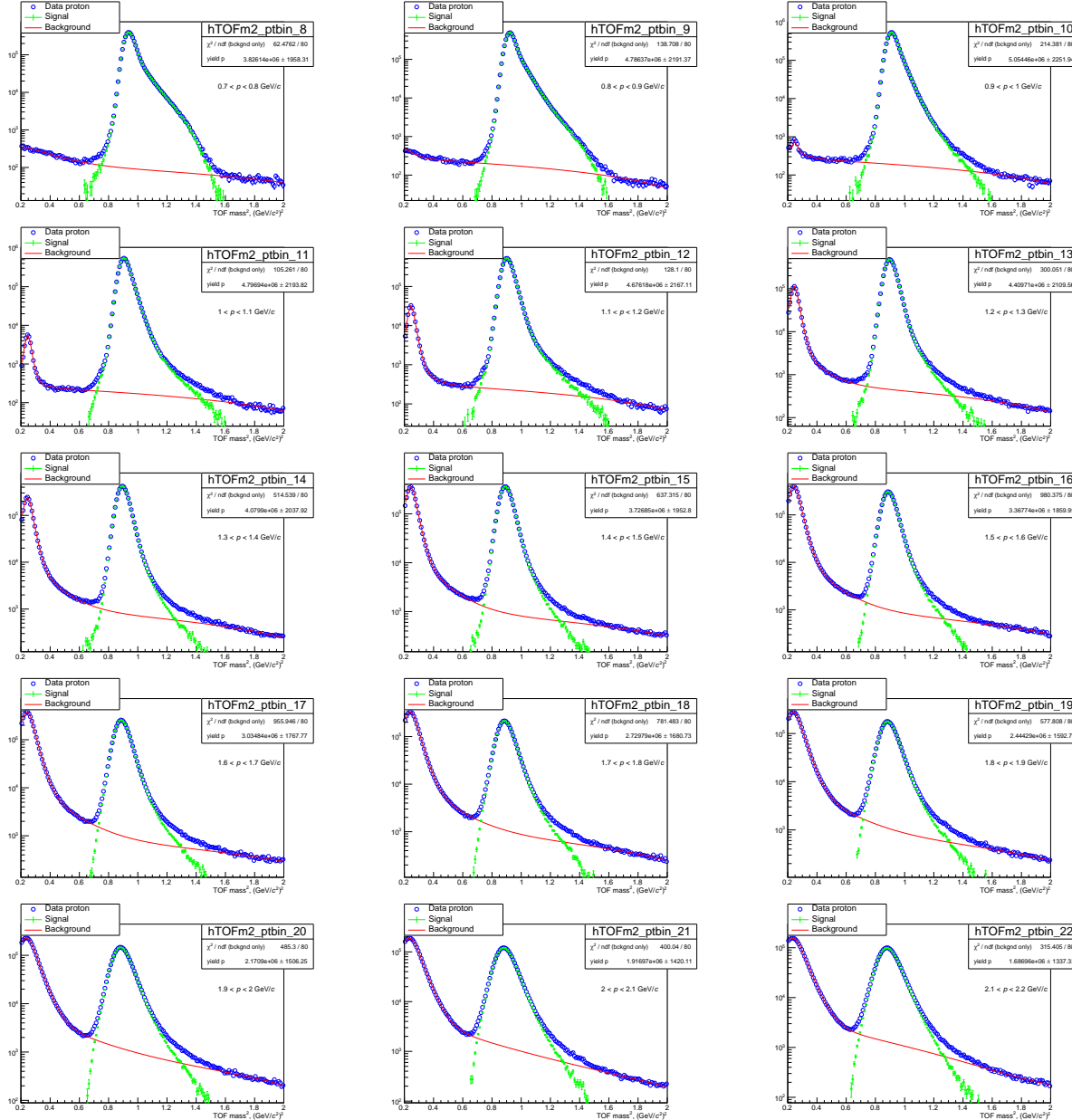
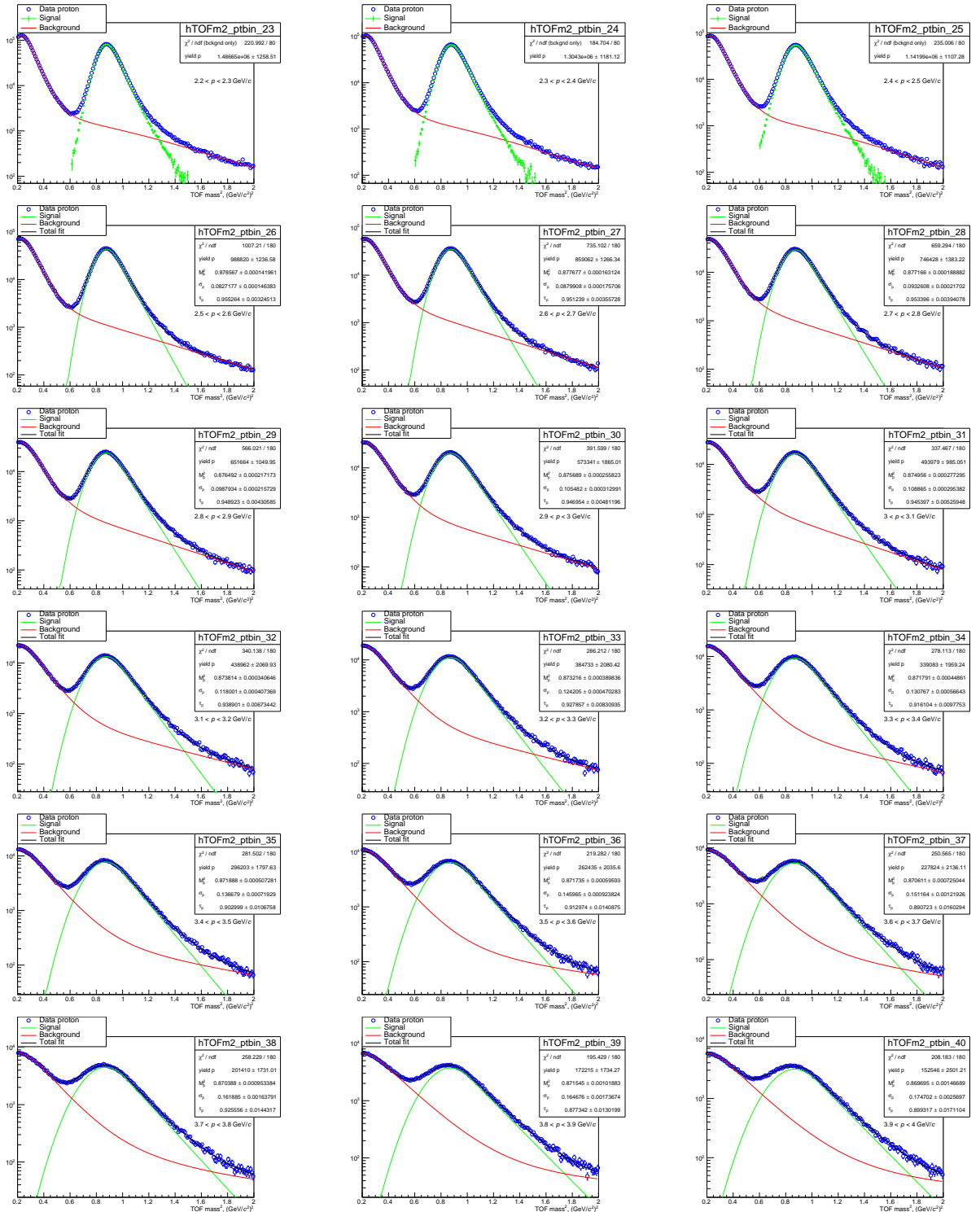


Fig. B.1: TOF m^2 fits of proton candidates in different momentum bins.

Fig. B.2: TOF m^2 fits of proton candidates in different momentum bins.

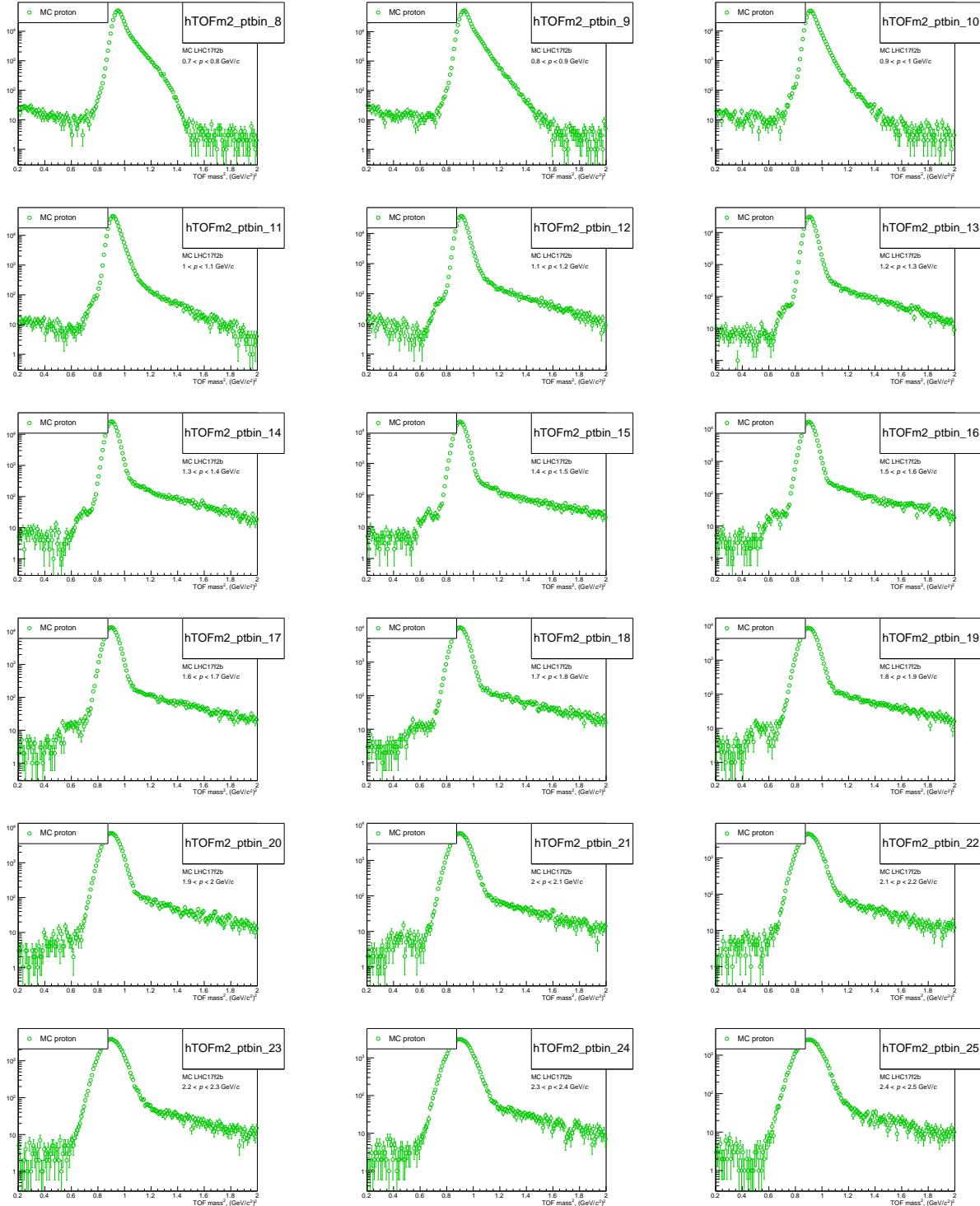


Fig. B.3: TOF m^2 distributions of primary protons in Monte Carlo simulations.

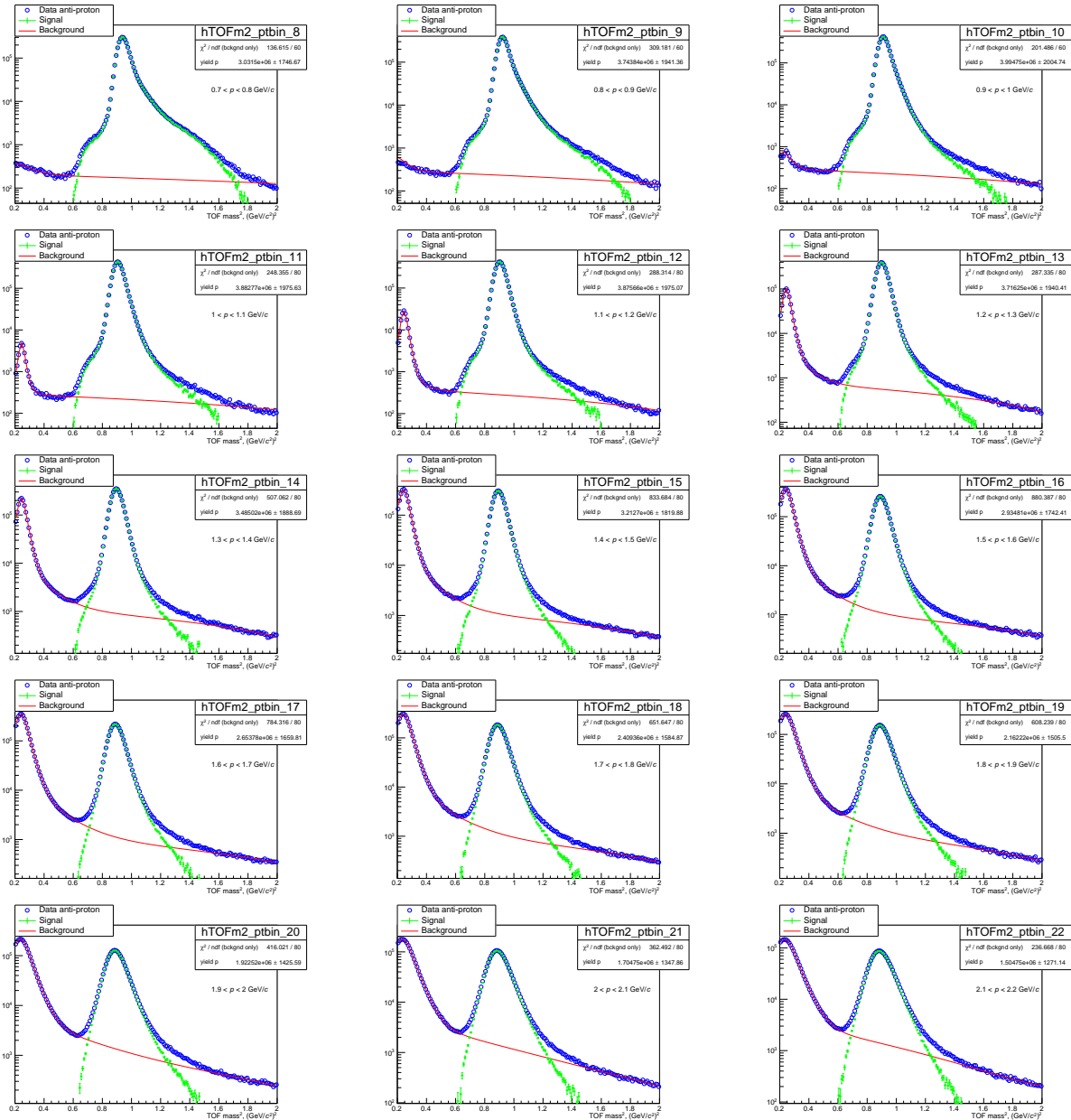


Fig. B.4: TOF m^2 fits of anti-proton candidates in different momentum bins.

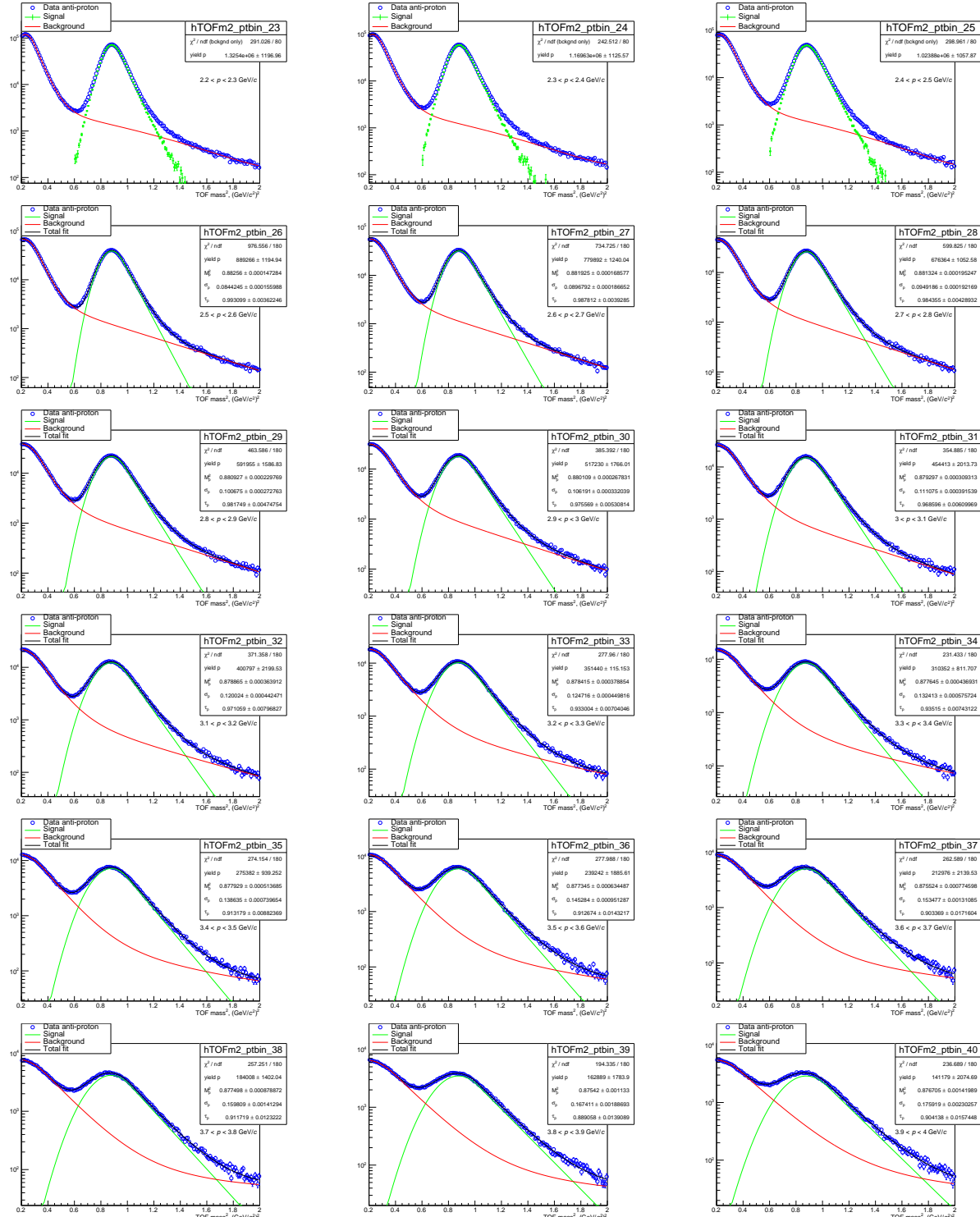


Fig. B.5: TOF m^2 fits of anti-proton candidates in different momentum bins.

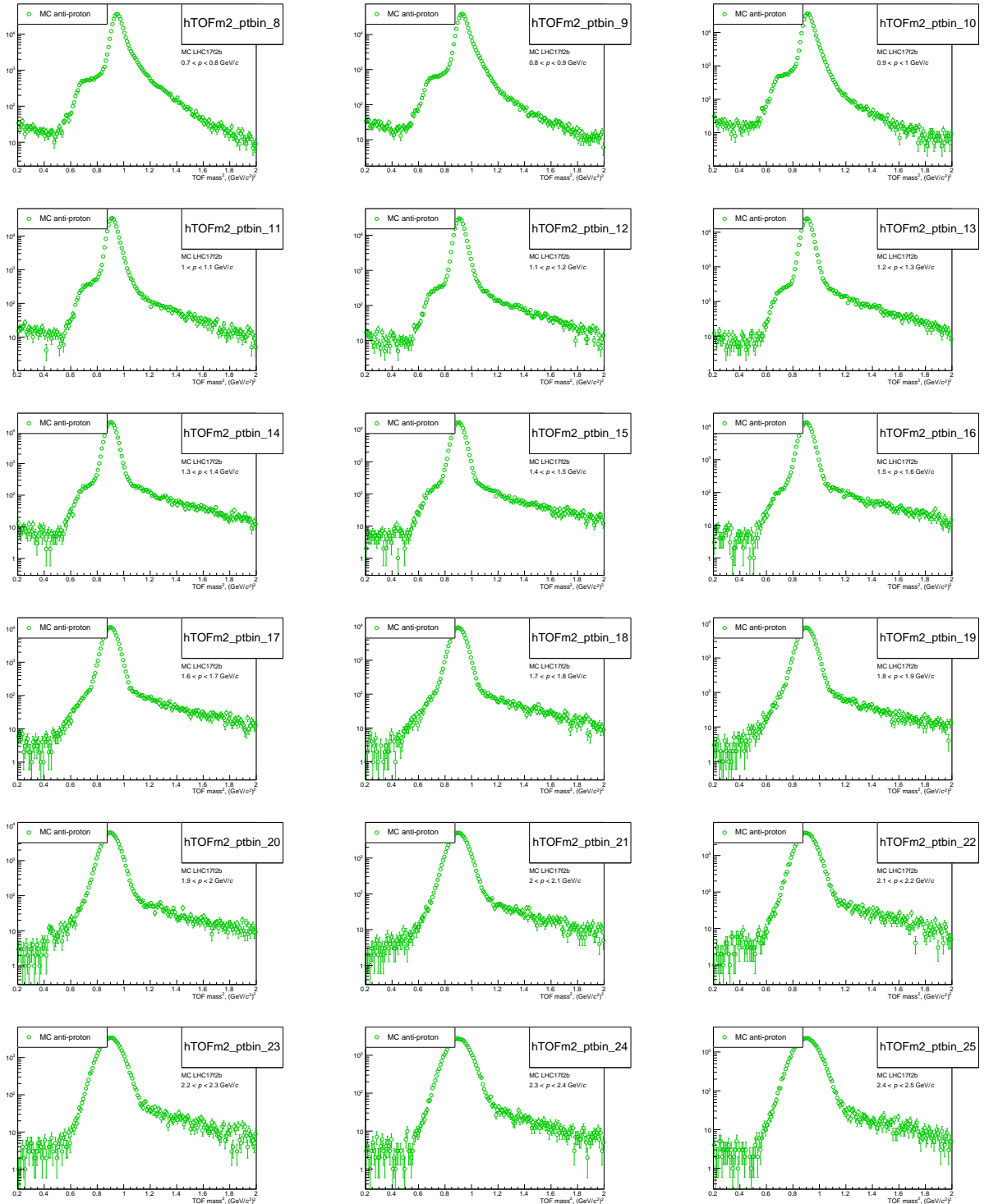


Fig. B.6: TOF m^2 distributions of primary anti-protons in Monte Carlo simulations.

474 B.2 TOF m^2 fits for (anti-)deuterons

475 Following figures show fits to TOF m^2 distributions of (anti-)deuteron candidates in all analysed momen-
 476 tumbum bins. The fit procedure is described in Section 4.1.

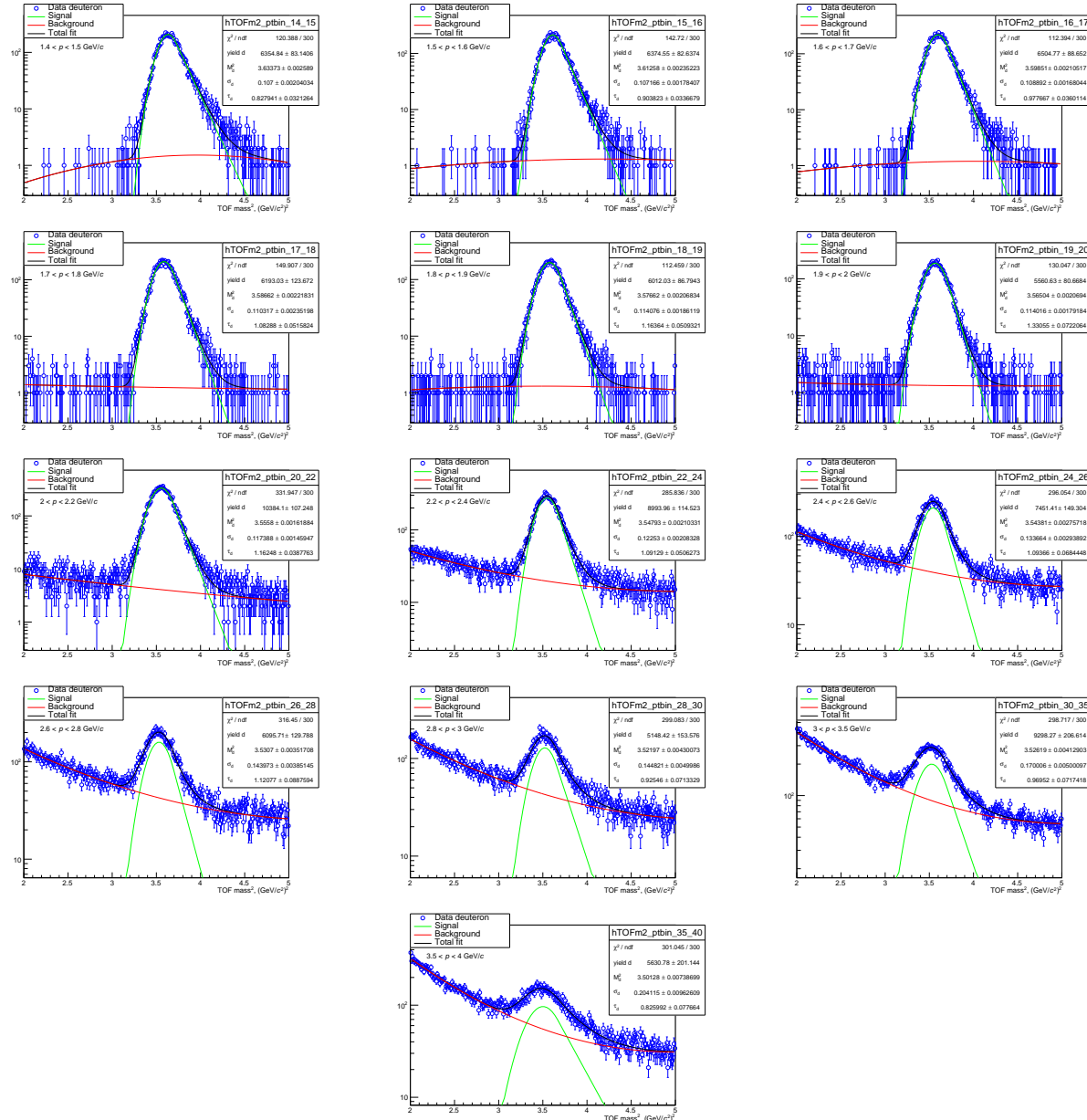
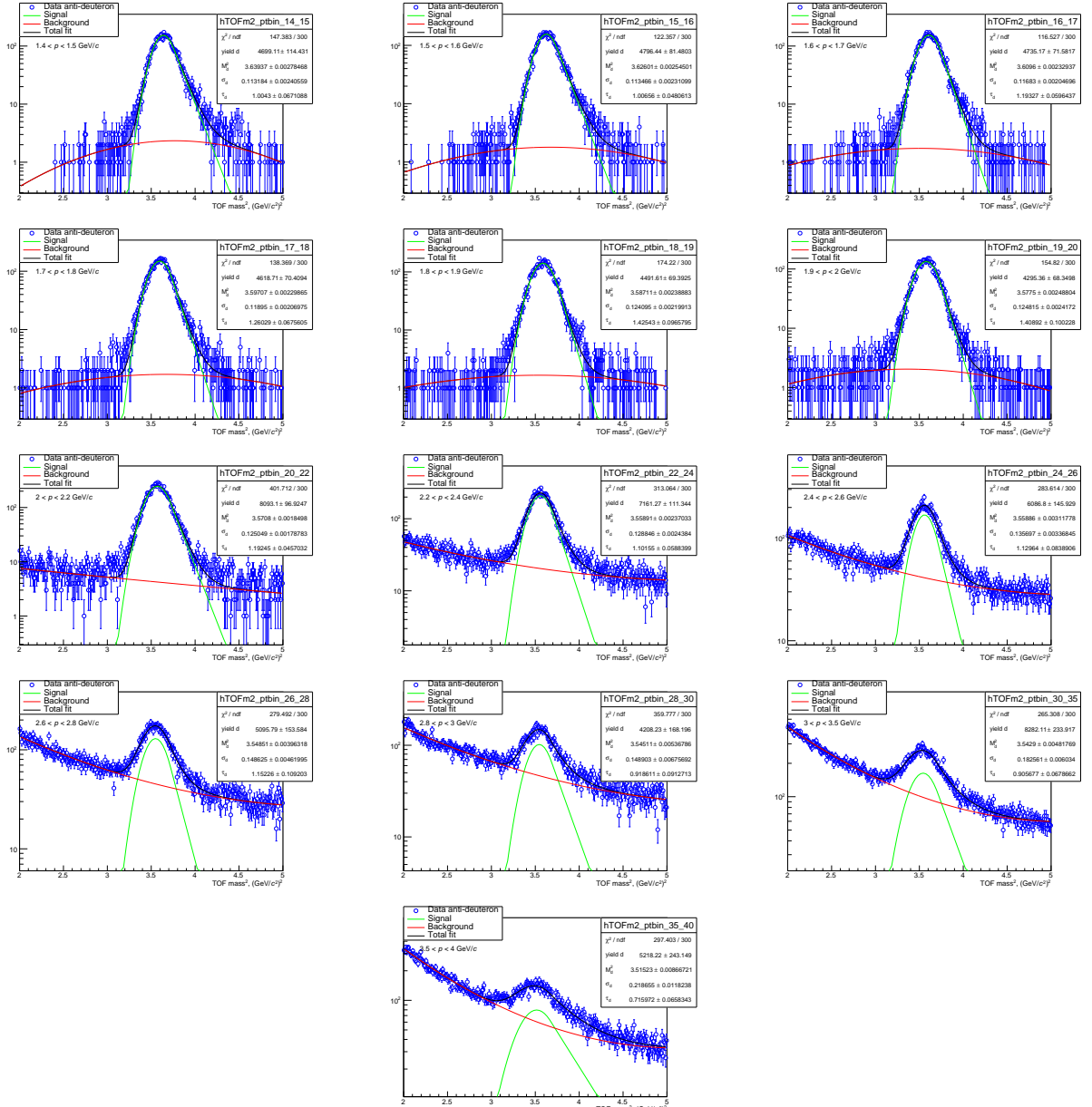


Fig. B.7: TOF m^2 fits of deuteron candidates in different momentum bins.

**Fig. B.8:** TOF m^2 fits of anti-deuteron candidates in different momentum bins.

477 **C DCA_{xy} fits**

478 **C.1 DCA_{xy} template fits for (anti-)protons**

479 Following figures show template fits to DCA_{xy} distributions of (anti-)proton candidates in different mo-
480 mentum bins. The fit procedure is described in Section 4.2.

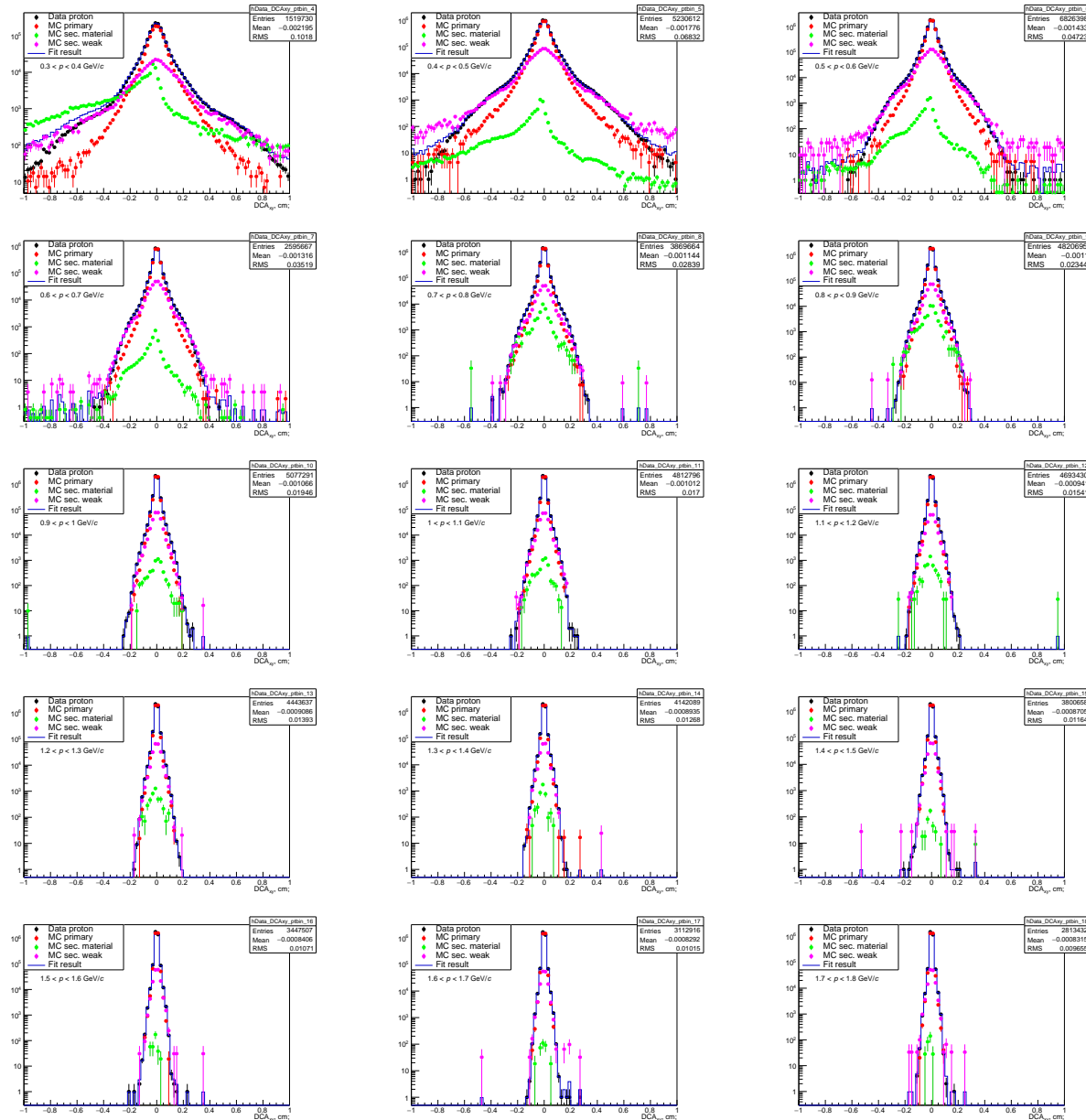
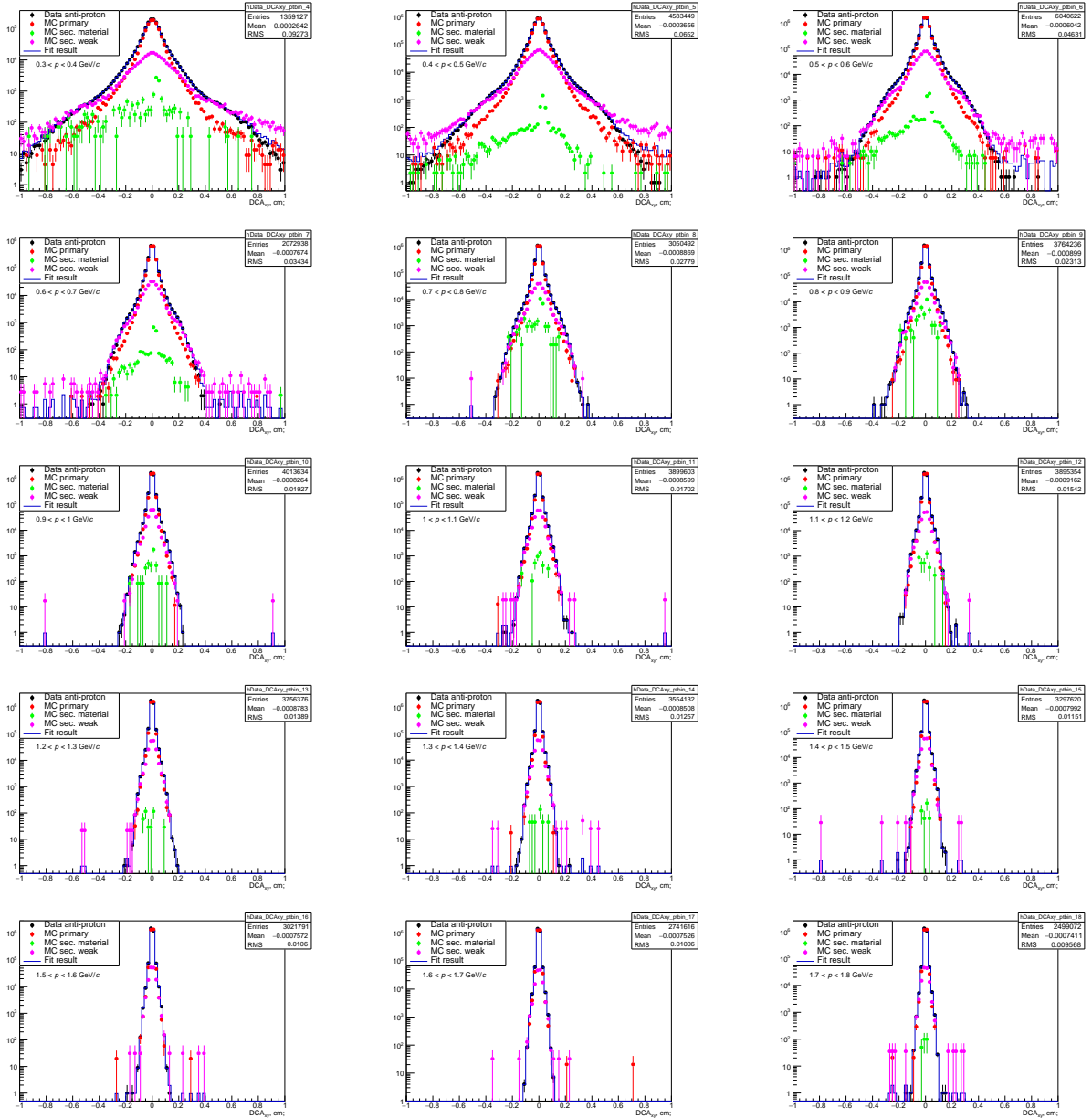


Fig. C.1: DCA_{xy} fits of proton candidates in different momentum bins.

Fig. C.2: DCA_{xy} fits of anti-proton candidates in different momentum bins.

481 C.2 DCA_{xy} fits for (anti-)deuterons

482 Following figures show fits to DCA_{xy} distributions of (anti-)deuteron candidates in different momentum
 483 bins. The fit procedure is described in Section 4.2. Since the fraction of secondary anti-deuterons is
 484 assumed to be zero, anti-deuteron DCA_{xy} distributions are fitted only with signal function (sum of two
 485 gaussians).

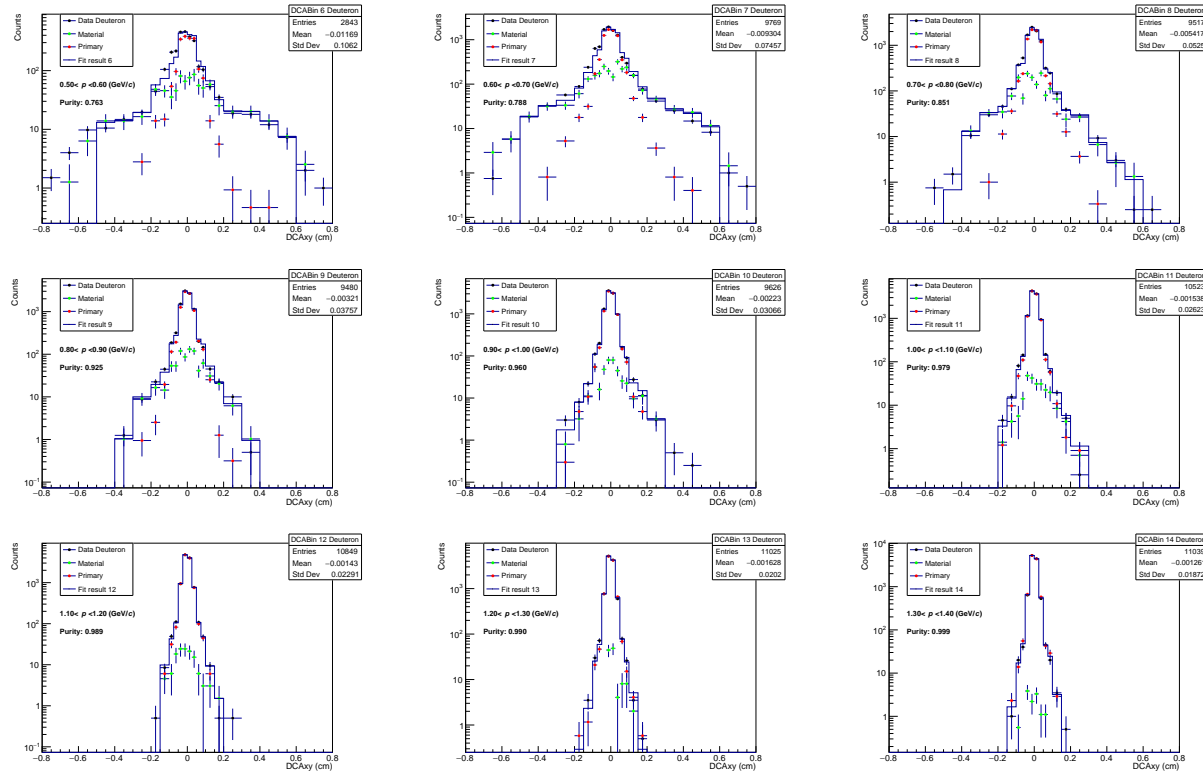


Fig. C.3: DCA_{xy} fits of deuteron candidates in different momentum bins.